

Image Reconstruction for Limited-Angle Electron Beam X-Ray Computed Tomography With Energy-Integrating Detectors for Multiphase Flows

Seongjin Yoon ¹, Simo A. Mäkiharju ², Jeffrey A. Fessler ³, *Fellow, IEEE*, and Steven L. Ceccio

Abstract—We propose a new iterative X-ray computed tomography (CT) reconstruction algorithm for electron beam X-ray tomography of multiphase flows in metal pipes. This application uses limited-angle projections due to the fixed configuration, and semiconductor-type energy-integrating detectors. For the data-fitting objective function, the proposed method incorporates a nonlinear Gaussian model with object-dependent variance to approximate the compound Poisson distribution, and a dual material decomposition based on images of the volume fractions of metal (titanium) and liquid (water). The volume fraction-based material decomposition enables us to use a maximum sum constraint that helps address the ill-posed nature of the problem. Two different regularizers, ℓ_0 norm and edge-preserving hyperbola regularizers, are applied differently on each volume fraction image based on the characteristics of objects in each image. A synthetic phantom simulation illustrates that the proposed algorithm enables the aforementioned CT system to achieve high quality images by minimizing artifacts induced by limited-angle data and beam hardening.

Index Terms—Electron beam X-ray tomography (EBXT), statistical reconstruction, limited-angle tomography, compound Poisson distribution.

I. INTRODUCTION

MODERN optical measurement techniques, such as particle image velocimetry (PIV), can quantify the velocity (and in some cases even pressure) field in most single phase fluid flows. However, conventional (near-visible) optical methods are not usable for most gas-liquid multiphase flows of interest due to refraction of light at the phase interfaces, which

even at low gas fractions make these flows opaque. To quantify velocity or phase distribution in multiphase flows, there have been a few attempts to use X-ray based 2D densitometry or 3D computed tomography (CT) techniques in fluid experiments [1]–[11]. The major challenge in applying X-ray CT to fluid flow measurement is temporal blurring. The flows of industrial and naval interest require measurements at rates much higher than required for most CT applications. Hence, conventional CT systems cannot be used for time resolved fluid visualization due to the excessive temporal blurring induced by the rapid motion. For faster scanning, electron beam X-ray tomography (EBXT) has been considered as a promising technology [1], [2], [5]–[8], [11]. EBXT can improve the temporal resolution when imaging moving objects by removing the mechanical rotation of the source and detector used in conventional X-ray CT. Instead of physically rotating a source and detector pair, EBXT deflects an electron beam by applying electro-magnetic fields to generate X-rays in a sequence of specific positions along the tungsten arc, while a fixed array of detectors acquires projection images as the beam sweeps the arc. Consequently, much higher scan rates are achievable than by conventional CT.

Although EBXT significantly enhances temporal resolution compared to conventional CT, it still has several drawbacks. Because of its fixed source-detector configuration, full-angle CT data requires angular overlap between the source target and the detector. The conventional solution was to place an axial offset between the source and the detector [2]. This axial displacement can generate artifacts due to the misalignment between the source and detector in 2-D CT as each projection scans different plane. Furthermore, 2-D array detectors are not easily usable for this configuration because the target blocks detectors. To solve the overlapping problem while enabling the use of 2-D array detectors, a tungsten coated graphite target was developed, enabling full-angle CT by making the X-ray source almost transparent to X-rays [5]. However, it is not yet available for commercial applications. Fig. 1 shows three different configurations of EBXT that avoid overlap. This paper focuses on reconstruction algorithms for limited angle EBXT because this configuration is readily implementable with commercially available components, and expandable to 3D CT as well.

Despite the advances in hardware to enable full-angle EBXT, not much attention has gone into the CT reconstruction algorithms for the limited angle EBXT. For limited angle CT

Manuscript received September 8, 2017; accepted November 14, 2017. Date of publication November 20, 2017; date of current version February 8, 2018. This work was supported in parts by the Office of Naval Research under Grant N00014-14-1-0292 and by the Bettis Atomic Power Laboratory under Contract DE-NR0000031. The associate editor coordinating the review of this manuscript and approving it for publication was Dr. Kees Joost Batenburg. (*Corresponding author: Seongjin Yoon.*)

S. Yoon and S. Ceccio are with the Department of Naval Architecture and Marine Engineering, University of Michigan, Ann Arbor MI 48109 USA (e-mail: seongjin@umich.edu; ceccio@umich.edu).

S. Mäkiharju is with the Department of Mechanical Engineering, University of California, Berkeley CA 94720 USA (e-mail: makiharju@berkeley.edu).

J. Fessler is with the Department of Electrical Engineering and Computer Science, University of Michigan, Ann Arbor MI 48109 USA (e-mail: fessler@umich.edu).

This paper has supplementary downloadable material available at <http://ieeexplore.ieee.org>.

Color versions of one or more of the figures in this paper are available online at <http://ieeexplore.ieee.org>.

Digital Object Identifier 10.1109/TCI.2017.2775603

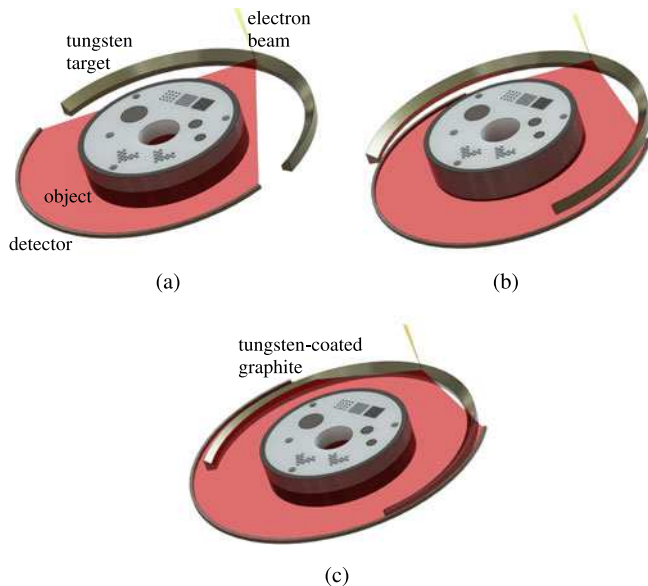


Fig. 1. Three types of EBXT source-detector configurations; (a) limited angle, (b) full angle with axial offset, (c) full angle with X-ray transparent target.

of two-phase flows, there have been attempts to improve the result image by thresholding binarization [1] and level-set binarization [11]. However, binarization can only be applied to images where all objects of significance have size larger than reconstruction resolution (i.e., voxel size). The size of objects (bubbles) in multiphase flows, particularly cavitating flows, ranges from microns to centimeters. In multi-phase fluid mechanics, a volume fraction approach is commonly used to account for smaller objects that cannot be fully resolved, where the material property is volume-averaged over each voxel [12]. With volume fraction approaches, each pixel can have any gray value (i.e., phase fraction) between 0 to 1. Applying binarization to flows having void fractions varying continuously from 0 to 1 can cause significant inaccuracy.

Numerous statistical reconstruction methods for poly-energetic source CT have been published. Among them, dual energy (DE) CT has been a popular method to account for the energy-dependent nonlinearity of the X-ray photon attenuation [13]–[35]. DECT acquisitions can be classified into four categories: dual source [15], fast kVp switching [28], dual layer detectors [36] and energy binning detectors [18]. Applying dual source or dual layer detector to the electron beam is difficult, as collimators cannot be used in EBXT because the incident angle of the beam changes along the scan. Fast kVp switching in EBXT would require synchronization between the sequences of beam voltage and deflection coils, and may not be achievable due to limitations of high voltage (HV) supply response time. Additionally, failed synchronization could cause the beam to hit the chamber walls, which could cause permanent damage in fractions of a second. To date, EBXT has used only for single energy CT, i.e., a single source voltage with energy-integrating detectors.

Achieving DECT-like results when using only the single bin energy-integrated data is not straightforward, especially when only limited angle projection data is available. Unlike the

Poisson maximum likelihood of photon counting detectors, less attention has gone into finding an accurate probabilistic model for energy-integrating detectors, and many existing iterative methods use conventional weighted least square (WLS) method for data-fitting (likelihood) objective functions [20], [33]. While WLS is a widely accepted method for high photon count rate, it could fail to accurately estimate parameters when photon count rates are low. Whiting *et al.* [37] showed that the compound Poisson distribution of the energy-integrating data matches well with the measured probability density function, and it quickly becomes Gaussian-like when the number of photons becomes greater than 20. That work also showed that the mean and the variance of the energy-integrating data has a linear relation. Recently, Lasio *et al.* [38] proposed a simple Poisson log likelihood for energy-integrating detectors using equivalent photon counts, i.e., total energy divided by the equivalent mean energy of incident photons. Although the simple Poisson model was accurate enough for a certain problem [38], its linear approximation does not fully reflect the nonlinear physics of the attenuation of photons.

This paper describes a way to take advantage of a dual material decomposition method similar to that used for the beam-hardening removal, while using energy-integrating detectors. To do this, we used the material decomposition method based on the volume fraction maps following [35], and a nonlinear Gaussian approximation (NGA) to simplify the aggregated compound Poisson distribution. Our probability model incorporates the spectral response of the detector crystals by using a simple Gaussian and tail mixture model suggested by Srivastava *et al.* [39]. While the system configuration considered and reconstruction method proposed are expandable to 3D, this paper focuses on reconstructing a single CT slice.

Estimating dual material volume fractions using only a single bin energy-integrated data leads to an ill-posed problem where the solution is not unique. However, employing the fraction map has a benefit as its physical constraints, i.e., non-negativity and the bounded sum, help to narrow the feasible domain. Even with the constraints, the solution is still not unique. We employ two regularizers, an edge-preserving and ℓ_0 norm regularizer to determine the solution. Based on the dual material decomposition, different regularizers are applied to the fraction maps depending on the characteristics of the materials.

II. SYSTEM DESCRIPTION

We designed the reconstruction algorithm and simulation conditions in this study focusing on the forthcoming hardware setup of the scanning electron beam X-ray tomography (SEBXT) for the multiphase flow experiments in the University of Michigan. Fig. 3 shows a schematic diagram of SEBXT. The X-ray source of SEBXT is based on the 150 kV 20 kW electron beam gun system with 170 degree tungsten target. We use 160 degree, 128 pixels arc shaped CdTe semiconductor detectors that convert X-ray photon energy to electrons directly without using scintillators. All other system specifications are summarized in Table I.

To evaluate the performance of the SEBXT with an emphasis on the industrial application such as boilers, we in-

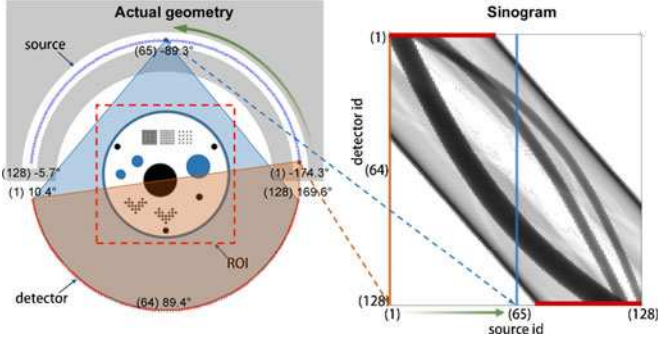


Fig. 2. (Left) Geometry of the source points, the detector points, and the region of interest; (Right) corresponding sinogram. The thick red lines in the sinogram indicate the regions beyond which data is missing due to the limited angle CT system.

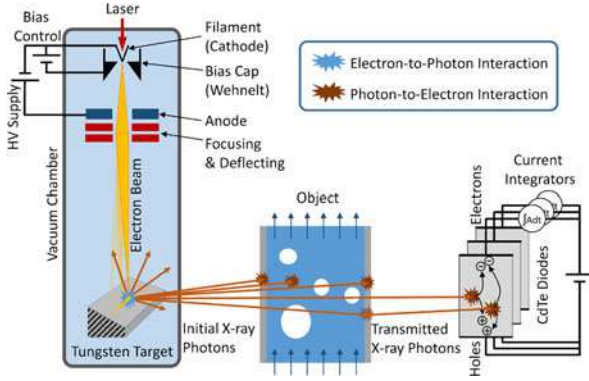


Fig. 3. Schematic diagram of an electron beam gun, tungsten target, object (titanium pipe with gas-liquid fluids), and energy-integrating detectors.

produce a synthetic phantom that consists of water-equivalent structure in a titanium pipe with three circular titanium rods and various sizes of bubbles, with bubble radius ranging from 0.05 cm to 1.125 cm. Fig. 4 shows the true image of the phantom, represented by volume fraction image of each material. The locations, sizes, and materials of the objects in the phantom are summarized in the supplement.

For simplicity, we assume that our measurement data H_i is total integrated X-ray photon energy obtained by linearly transforming the integrated current over exposure time along the i th source-detector pair.

III. RECONSTRUCTION METHODS

For current mode (energy-integrating) semiconductor type detectors with a polyenergetic source, the actual distribution of the energy transferred to the detector by photons falls into the sum of independent compound Poisson random variables, called the aggregated compound Poisson random variable [40], which is not practically applicable for the iterative maximum likelihood estimator due to its complicated form. As a common approach, the distribution of the measurement data H_i of the current mode detector is approximated by the normal distribution [40], [41], and [42]:

$$H_i \sim \mathcal{N}(\eta(\bar{y}_i), \sigma^2(\bar{y}_i)), \quad (1)$$

TABLE I
SEBXT SYSTEM SPECIFICATION

Source	
Type	electron beam gun
Voltage	150 kV
Current	133 mA
Target material	tungsten
Target radius	80 mm
Range of angles	170 degrees
Number of projections	128
Scanning speed	1000 scans/second
Detector	
Type	semiconductor
Mode	current-integrating
Material	CdTe
Radius	80 mm
Range of angles	160 degrees
Number of pixels	128
Face area	$1.33 \times 1.33 \text{ mm}^2$
Exposure time	$1.95 \times 10^{-6} \text{ sec}$
Reconstruction image	
Field of view	$90 \times 90 \text{ mm}^2$
Total pixels	192×192

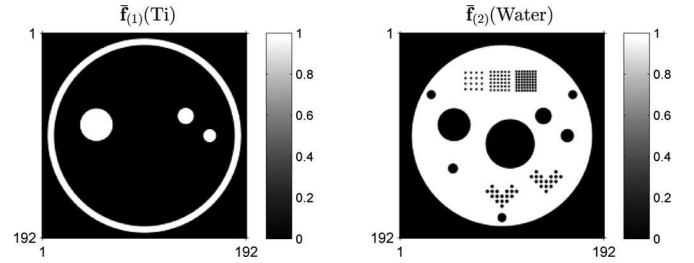


Fig. 4. True volume fraction images of the phantom

where η is the mean of the measurement data H , σ^2 is the variance of H , i is the index of rays, and \bar{y}_i is the ideal expected transmitted X-ray photon counts at the i th ray. Note that the estimator based on (28) differs from conventional WLS methods, as the variance also depends on \bar{y}_i . We refer to this approach as the nonlinear Gaussian approximation (NGA) hereinafter. After discretizing the continuous X-ray photon energy level \mathcal{E} into N_k bins with an interval $\Delta\mathcal{E}$, we define $\bar{y}_i(\mathcal{E}_k)$ as the ideal expected photon counts at the i th ray and the k th energy bin based on the Beer's law:

$$\bar{y}_i(\mathcal{E}_k) \equiv \int_{\mathcal{E}_k - 1/2\Delta\mathcal{E}}^{\mathcal{E}_k + 1/2\Delta\mathcal{E}} I_i^0(\mathcal{E}) \exp\left(-\int_{\mathcal{L}_i} \mu(\mathbf{x}, \mathcal{E}) dl\right) d\mathcal{E}, \quad (2)$$

where k is the energy level index, $\Delta\mathcal{E}$ is the interval between energy levels, $I_i^0(\mathcal{E})$ is the continuous initial emission spectrum, $\int_{\mathcal{L}_i} \cdot dl$ is the line integral along the i th ray, and $\mu(\mathbf{x}, \mathcal{E})$ is the attenuation coefficient at the spatial location \mathbf{x} and energy \mathcal{E} .

The main goal of the following section is to define the analytic expression of η and σ^2 , apply the maximum likelihood estimation, and lastly, solve it iteratively using a majorization-minimization algorithm specifically designed for the given likelihood function.

A. Basis Material Decomposition

In (2), attenuation coefficient $\mu(\mathbf{x}, \mathcal{E})$ is a function of both space and energy. For the sake of simplicity, we first decompose it into the energy-dependent term and space-dependent term. Sukovic and Clinthorne [17], [19], [20] suggested a decomposition method to split the attenuation coefficient into the mass attenuation coefficient which depends on energy, and the local density which depends on space, as follows:

$$\mu(\mathbf{x}, \mathcal{E}) = \sum_{l=1}^{N_l} \beta_l(\mathcal{E}) \rho_l(\mathbf{x}), \quad (3)$$

where N_l is the total number of materials in the object. This study uses a dual material decomposition model: $N_l = 2$. $\beta_l(\mathcal{E})$ is the known mass attenuation coefficient of the l th material at energy level \mathcal{E} , and $\rho_l(\mathbf{x})$ is the local density at the spatial location \mathbf{x} . Elbakri and Fessler [25] further decomposed the density map into actual material density and fraction map,

$$\mu(\mathbf{x}, \mathcal{E}) = \sum_{l=1}^{N_l} \beta_l(\mathcal{E}) \rho(\mathbf{x}) f_l(\rho(\mathbf{x})). \quad (4)$$

In this model, material fraction is assumed to be a function of the density, where the function can be obtained by the empirical curve fitting based on the known material data. While this approach can be used for the specific field where there is a strong relationship between the density and fraction, it cannot be applied to more general case where the fraction is not a one-to-one function of the density. Instead, Long and Fessler [35] introduced a modified volume fraction method in which the fraction is independent of the density:

$$\mu(\mathbf{x}, \mathcal{E}) = \sum_{l=1}^{N_l} \beta_l(\mathcal{E}) \rho_l f_l(\mathbf{x}). \quad (5)$$

This type of decomposition can facilitate applying physical constraints. For example, if all materials in the object are considered in the reconstruction, we can set the constraint $\sum_l f_l(\mathbf{x}) = 1$ for any \mathbf{x} . This sum-to-one constraint is called volume conservation. Usually, X-ray attenuation due to air is negligibly small, thus the attenuation of the air is assumed to be zero. Then, we can set the constraint $\sum_l f_l(\mathbf{x}) \leq 1$ for any \mathbf{x} , excluding the air fraction. This volume fraction-sum constraint (VFSC) significantly improves the quality of reconstructed images for limited angle CT, as shown later.

Finally, discretize $\mu(\mathbf{x}, \mathcal{E})$ using the piecewise constant basis in energy,

$$\mu(\mathbf{x}, \mathcal{E}_k) = \sum_{l=1}^{N_l} u_l(\mathcal{E}_k) f_l(\mathbf{x}), \quad (6)$$

where $u_l(\mathcal{E}_k) = u_{(k,l)} = \beta_l(\mathcal{E}_k) \rho_l$. After discretizing $f_l(\mathbf{x})$ in space, and plugging (6) into (2), the discretized average photon flux $\bar{y}_{(i,k)}$ is written as:

$$\bar{y}_{(i,k)} = I_{(i,k)}^0 \exp\left(-\sum_{l=1}^{N_l} u_{(k,l)} [\mathbf{A}\mathbf{f}_{(l)}]_i\right) \Delta\mathcal{E}, \quad (7)$$

where $I_{(i,k)}^0 = I_i^0(\mathcal{E}_k)$, $[t]_i$ is the i th element of the vector $\mathbf{t} \in \mathbb{R}^{N_i}$, $\mathbf{A} \in \mathbb{R}^{N_i \times N_j}$ is the projection matrix with its element $a_{(i,j)}$ being the Radon transform of the j th spatial basis along the i th ray, and $\mathbf{f}_{(l)} = [f_{(1,l)}, \dots, f_{(N_j,l)}]'$, where $[\cdot]'$ denotes transpose. N_i and N_j are the number of rays and the number of image pixels in space, respectively.

B. Photon Energy Detection Statistics for Current Mode Detectors

To obtain statistical properties $\bar{\eta}$ and σ^2 for the total photon energy probability density function (PDF), assume that the event of the photo-electric interaction of each photon is independent, and number of X-ray photons at each discretized energy level follows independent Poisson distribution.

$$Y_{(i,k)} \sim \text{Poisson}(\bar{y}_{(i,k)}), \quad (8)$$

where the parameter (mean) $\bar{y}_{(i,k)}$ is defined in (7).

Then, a mathematical model is needed to compute the PDF of energy transferred to the detector for each photon of the discrete energy level \mathcal{E}_k , which is interpreted as the spectral response $\mathcal{B}(\mathcal{E}_k)$ of the detector. Semiconductor type energy-integrating detectors measure total integrated energy of X-ray photons by recording the current induced by photoelectrons when photons interact with the semiconductor. Probability of photon-electron interaction depends on many factors, such as the size and material of the detector, and it is hard to compute analytically. Instead, Srivastava *et al.* [39] suggested a simplified empirical model for $\mathcal{B}(\mathcal{E})$ as a mixture of Gaussian photo-peak and uniform continuum:

$$\mathcal{B}(\mathcal{E}'; \mathcal{E}) = w_{\mathcal{E}} \mathcal{B}_G(\mathcal{E}'; \mathcal{E}, \sigma_{\mathcal{E}}) + (1 - w_{\mathcal{E}}) \mathcal{B}_C(\mathcal{E}'; \mathcal{E}), \quad (9)$$

$$\mathcal{B}_G(\mathcal{E}'; \mathcal{E}) = \frac{1}{\sqrt{2\pi}\sigma_{\mathcal{E}}} \exp\left(-\frac{(\mathcal{E}' - \mathcal{E})^2}{2\sigma_{\mathcal{E}}^2}\right), \quad (10)$$

$$\mathcal{B}_C(\mathcal{E}'; \mathcal{E}) = \begin{cases} 1/\mathcal{E} & \text{if } 0 \leq \mathcal{E}' \leq \mathcal{E} \\ 0 & \text{otherwise} \end{cases}, \quad (11)$$

$$\sigma_{\mathcal{E}} = k\sqrt{\mathcal{E}}. \quad (12)$$

Here, $w_{\mathcal{E}}$ is the mixture probability of photo-electric interaction, and k is the variance coefficient. Without conducting experiments with multiple monoenergetic sources, estimating k and $w_{\mathcal{E}}$ of the detector by experiment is impossible. For the simulation purpose, we extracted $w_{\mathcal{E}}$ from the existing efficiency data of the commercial 1 mm thick CdTe detector provided by Amptek [43]. Fig. 5 shows estimated $w_{\mathcal{E}}$ for 1 mm thick commercial CdTe semiconductor detector. Note that $w_{\mathcal{E}}$ depends on both the material and the size of the detector, and estimated values of $w_{\mathcal{E}}$ in Fig. 5 are for the simulation only. For actual data reconstruction, $w_{\mathcal{E}}$ must be tuned to fit the spectral response of the specific detectors. In general, CdTe detector shows good efficiency at low energy, then gradually loses its efficiency after the energy higher than 100 keV.

Denote $E_m(\mathcal{E})$ as the energy transferred to the detector from m th photon which originally had energy \mathcal{E} . As noted before,

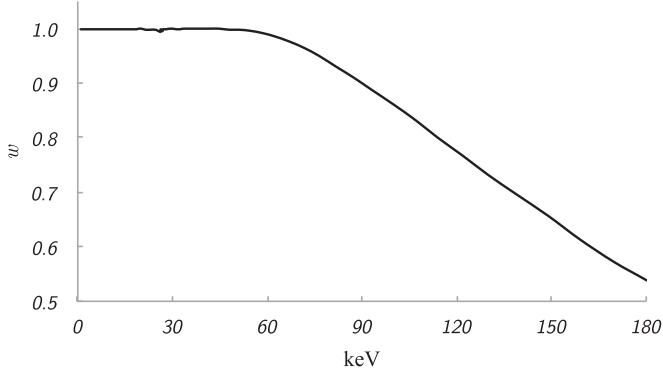


Fig. 5. Mixture weight of photo-electric interaction $w_{\mathcal{E}}$ of 1 mm CdTe detector (based on the efficiency data from Amptek XR-100T-CdTe [43]).

energy transferring events at the detector are assumed to be independent, then $E_m(\mathcal{E})$ can be seen as independent and identically distributed (i.i.d.) random variables that have the spectral response function as their PDFs,

$$E_m(\mathcal{E}) \stackrel{\text{i.i.d.}}{\sim} \mathcal{B}(\cdot; \mathcal{E}). \quad (13)$$

To get $\bar{\eta}$ and σ^2 , we first need to compute the first, second, and third moment of $E_m(\mathcal{E})$ using (9) to (12),

$$m_E^{(1)} \equiv \mathbb{E}[E_m; \mathcal{E}] = \frac{w_{\mathcal{E}} + 1}{2} \mathcal{E}, \quad (14)$$

$$m_E^{(2)} \equiv \mathbb{E}[E_m^2; \mathcal{E}] = w_{\mathcal{E}} \sigma_{\mathcal{E}}^2 + \frac{2w_{\mathcal{E}} + 1}{3} \mathcal{E}^2, \quad (15)$$

$$m_E^{(3)} \equiv \mathbb{E}[E_m^3; \mathcal{E}] = 3w_{\mathcal{E}} \mathcal{E} \sigma_{\mathcal{E}}^2 + \frac{3w_{\mathcal{E}} + 1}{4} \mathcal{E}^3. \quad (16)$$

Let T_i be the total energy transferred to the i th detector from the monoenergetic beam with energy level \mathcal{E}_k , then T_i can be written as the compound Poisson random variable, i.e., sum of the i.i.d. random variables where the total number is Poisson random variable:

$$T_i(\mathcal{E}_k) = \sum_{m=1}^{Y_i} E_m(\mathcal{E}_k). \quad (17)$$

The mean, variance, and skewness of $T_i(\mathcal{E}_k)$ can be computed using the moments of $E_m(\mathcal{E}_k)$ in (14) to (16) as

$$\mathbb{E}[T_i(\mathcal{E}_k)] = \bar{y}_{(i,k)} m_{E_k}^{(1)}, \quad (18)$$

$$\text{Var}[T_i(\mathcal{E}_k)] = \bar{y}_{(i,k)} m_{E_k}^{(2)}, \quad (19)$$

$$\text{Skew}[T_i(\mathcal{E}_k)] = \frac{m_{E_k}^{(3)}}{\sqrt{\bar{y}_{(i,k)} \left(m_{E_k}^{(2)}\right)^3}}. \quad (20)$$

Details to obtain the statistical properties of the compound Poisson random variables can be found in [40]. For the polyenergetic beam, assume that all $T_i(\mathcal{E}_k)$ at different discretized energy levels are mutually independent. Then the sum $H_i = \sum_{k=1}^{N_k} T_i(\mathcal{E}_k)$ becomes the aggregated compound Poisson random variable

[40], and its statistical properties are

$$\mathbb{E}[H_i] = \sum_{k=1}^{N_k} \bar{y}_{(i,k)} m_{E_k}^{(1)}, \quad (21)$$

$$\text{Var}[H_i] = \sum_{k=1}^{N_k} \bar{y}_{(i,k)} m_{E_k}^{(2)}, \quad (22)$$

$$\text{Skew}[H_i] = \frac{\sum_{k=1}^{N_k} \bar{y}_{(i,k)} m_{E_k}^{(3)}}{\left(\sum_{k=1}^{N_k} \bar{y}_{(i,k)} m_{E_k}^{(2)}\right)^{3/2}}, \quad (23)$$

where $\bar{y}_{(i,k)}$ is defined in (7).

Since skewness of H_i is non-zero, approximating PDF of H_i requires at least a three-parameter distribution model to satisfy all the mean, variance and skewness at the same time. Shifted gamma distribution is known to be a good candidate to estimate the compound Poisson distribution [40], defined as

$$G^{tr}(h; h^{(0)}, a, b) = G(h - h^{(0)}; a, b), \quad (24)$$

where G is the two-parameter gamma distribution. a and b are the shape and rate parameters of the two-parameter gamma distribution, respectively. $h^{(0)}$ is the mean-shifting parameter. To find the parameters that satisfy the statistical properties described in (21), (22) and (23), first find a and b from the variance and skewness, then find $h^{(0)}$ to satisfy the mean by shifting the two-parameter gamma distribution. Then, we get the following analytic expressions for the shifted gamma approximation:

$$a_i = 4 \frac{\left(\sum_{k=1}^{N_k} \bar{y}_{(i,k)} m_{E_k}^{(2)}\right)^3}{\left(\sum_{k=1}^{N_k} \bar{y}_{(i,k)} m_{E_k}^{(3)}\right)^2}, \quad (25)$$

$$b_i = 2 \frac{\sum_{k=1}^{N_k} \bar{y}_{(i,k)} m_{E_k}^{(2)}}{\sum_{k=1}^{N_k} \bar{y}_{(i,k)} m_{E_k}^{(3)}}, \quad (26)$$

$$h_i^{(0)} = \sum_{k=1}^{N_k} \bar{y}_{(i,k)} m_{E_k}^{(1)} - \frac{a_i}{b_i}. \quad (27)$$

Even though the shifted gamma distribution can approximate the given compound Poisson approximation accurately, developing maximum likelihood for the X-ray CT which has massive amount of parameters to be estimated is not feasible due to the complicated digamma functions. Hence, we need some sort of simpler distribution model to design the estimator. As mentioned earlier, Gaussian distribution is chosen in the hope of the central limit theorem. Naive Gaussian approximation based on the mean (21) and the variance (22) are

$$H_i \sim \mathcal{N}(\eta(\bar{\mathbf{y}}_i), \sigma^2(\bar{\mathbf{y}}_i)), \quad (28)$$

$$\eta(\bar{\mathbf{y}}_i) = \sum_{k=1}^{N_k} \bar{y}_{(i,k)} m_{E_k}^{(1)}, \quad (29)$$

$$\sigma^2(\bar{\mathbf{y}}_i) = \sum_{k=1}^{N_k} \bar{y}_{(i,k)} m_{E_k}^{(2)}, \quad (30)$$

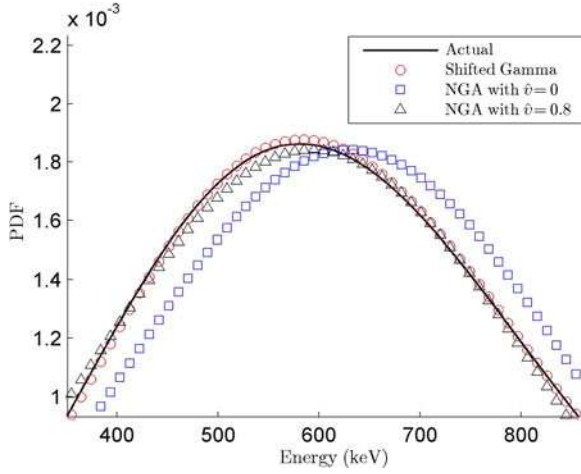


Fig. 6. Comparison of the probability density functions for the energy transferred to the detector by bichromatic X-ray photons at FWHM region, $\bar{y}(\mathcal{E}_1) = 10$, $\bar{y}(\mathcal{E}_2) = 5$, $\mathcal{E}_1 = 20$, $\mathcal{E}_2 = 100$, $w_1 = w_2 = 0.8$, $k = 0.5$, $v = 0.8$.

where $\bar{\mathbf{y}}_i = [\bar{y}_{(i,1)}, \dots, \bar{y}_{(i,N_k)}]'$. Due to the skewness error, maximum likelihood estimation of Gaussian approximation always give a biased result as the mean and the mode of the compound Poisson distribution are not in the same place. The difference between the mean and the mode can be seen in Fig. 6 where the mean is at the peak of the Gaussian distribution, and the mode is at the peak of the gamma or actual distribution. Thus, we want to move the mean of the Gaussian distribution close to the mode. For $\alpha_i > 1$, the difference between the mode and the mean can be found from the approximated shifted gamma distribution:

$$\begin{aligned} \mathbb{E}[H_i] - \text{mode}[H_i] &= \left(\frac{a_i}{b_i} + t_{0i} \right) - \left(\frac{a_i - 1}{b_i} + t_{0i} \right) \\ &= \frac{1}{b_i}. \end{aligned} \quad (31)$$

In terms of maximum likelihood, shifting the mean of Gaussian distribution onto the mode of the actual distribution increases the accuracy of the estimation when the data is close to the mode, but it also decreases the accuracy when the data is away from the mode. As a trade off, we chose a parameter \hat{v} that minimizes the mean-squared error between the actual distribution and the Gaussian approximation within the full-width at half maximum (FWHM) region as:

$$H_i \sim \mathcal{N} \left(\eta(\bar{\mathbf{y}}_i) - \hat{v} \frac{1}{b(\bar{\mathbf{y}}_i)}, \sigma^2(\bar{\mathbf{y}}_i) \right), \quad (32)$$

$$\hat{v}_i = \arg \min_v \int_{\text{HM}^-}^{\text{HM}^+} \left(p_{\text{true}_i}(h) - p_{H_i}(h; \eta_i, b_i, \sigma_i^2, v) \right)^2 dh, \quad (33)$$

where p_{true_i} is the actual marginal PDF, p_{H_i} is the Gaussian approximated marginal PDF, $\eta_i = \eta(\bar{\mathbf{y}}_i)$, $b_i = b(\bar{\mathbf{y}}_i)$, $\sigma_i^2 = \sigma^2(\bar{\mathbf{y}}_i)$, HM⁻ and HM⁺ indicate low and high FWHM bound. Finding explicit expression for the optimal \hat{v}_i is difficult as the

actual distribution p_{true} has a complicated form. For the results in this paper, we selected \hat{v} from the numerical experiments as the fixed constant $\hat{v} = 0.8$. This value suffices as there are many other uncertainties that can exceed the approximation error of using a constant \hat{v} value.

To validate the NGA model in (1), we obtained an analytic expression of the total energy PDF from the following recursive auto-convolution equation [37]. For a monoenergetic beam,

$$\begin{aligned} p_{T_i}(\mathcal{E})(t) &= \sum_{y=1}^{\infty} p_{T_i|Y_i}(\mathcal{E})(t|Y_i(\mathcal{E}) = y) \\ &\quad \cdot \Pr(Y_i(\mathcal{E}) = y) \\ &= \sum_{y=1}^{\infty} \left(p_{T_i|Y_i}(\mathcal{E})(t|Y_i(\mathcal{E}) = y-1) \right. \\ &\quad \left. * p_{T_i|Y_i}(\mathcal{E})(t|Y_i(\mathcal{E}) = 1) \right) \\ &\quad \cdot \Pr(Y_i(\mathcal{E}) = y). \end{aligned} \quad (34)$$

where $*$ denotes 1-D convolution with respect to t . For a polyenergetic beam,

$$\begin{aligned} p_{H_i}(t) &= p_{\sum_k T_i(\mathcal{E}_k)}(t) \\ &= \left(p_{T_i(\mathcal{E}_1)} * p_{T_i(\mathcal{E}_2)} * \dots * p_{T_i(\mathcal{E}_K)} \right)(t). \end{aligned} \quad (35)$$

Fig. 6 compares the analytic compound Poisson, shifted Gamma approximation, NGA, and NGA with mean correction for the case of bichromatic beam at FWHM region of the actual distribution. Note that the mean total number of photons is 15 in this case, which is equivalent to the worst case of the actual mean number of photons of our EBXT machine.

Finally, assuming readout noises r_i are additive and independent, then η and σ^2 follow from the linearity of the expectation and the variance of independent random variables:

$$H_i \sim \mathcal{N} \left(\eta(\bar{\mathbf{y}}_i) - \hat{v} \frac{1}{b(\bar{\mathbf{y}}_i)} + \bar{r}_i, \sigma^2(\bar{\mathbf{y}}_i) + \sigma_{r_i}^2 \right), \quad (36)$$

where \bar{r}_i and $\sigma_{r_i}^2$ are the mean and variance of the readout noise r_i , respectively.

C. Maximum Likelihood Estimation

For simplicity, we drop readout noise terms hereinafter. We assume the detector signals are mutually independent, so that the joint PDF is a product of marginal PDFs derived from (32) as follows:

$$p_{H_i}(h_i; \eta_i, b_i, \sigma_i) = \frac{1}{\sqrt{2\pi} \sigma_i^2} \exp \left(-\frac{(h_i - \eta_i + \hat{v}/b_i)^2}{2\sigma_i^2} \right), \quad (37)$$

where h_i is the measurement data of i th ray.

After taking the negative log of p_{H_i} and discarding constant terms, the proposed data-fitting objective function $\Psi_L(\bar{\mathbf{y}})$ is

defined as follows:

$$\Psi_L(\bar{\mathbf{y}}) = \sum_{i=1}^{N_i} \psi_L(\bar{\mathbf{y}}_i), \quad (38)$$

$$\psi_L(\bar{\mathbf{y}}_i) = \frac{1}{2} \left(\log \sigma_i^2(\bar{\mathbf{y}}_i) + \frac{(h_i - \eta_i(\bar{\mathbf{y}}_i) + \hat{v}/b_i(\bar{\mathbf{y}}_i))^2}{\sigma_i^2(\bar{\mathbf{y}}_i)} \right). \quad (39)$$

The data-fitting function $\Psi_L(\bar{\mathbf{y}})$ in (38) is not convex. Like all non-convex problems, iterative solution could be trapped in a local minimum, thus we need to choose an initial condition carefully to avoid any undesired local minima. In our case, we set the initial estimate to be the true titanium pipe image fully filled with water, which we found worked adequately in practice.

As shown in (7), $\bar{\mathbf{y}}$ is a function of the fraction image $\mathbf{f} = [\mathbf{f}'_{(1)}, \dots, \mathbf{f}'_{(N_i)}]'$. Consequently, we want to find \mathbf{f} that minimizes the data-fitting function in (39):

$$\hat{\mathbf{f}} = \arg \min_{\mathbf{f} \in \mathbb{F}} \Psi_L(\bar{\mathbf{y}}(\mathbf{f})), \quad (40)$$

where \mathbb{F} is the volume fraction constraint set:

$$\mathbb{F} = \left\{ \mathbf{f} \in \mathbb{R}^{N_j N_l} \mid f_{(j,l)} \geq 0, \sum_l f_{(j,l)} \leq 1 \right. \\ \left. \text{for } j = 1, \dots, N_j \text{ and } l = 1, \dots, N_l \right\}. \quad (41)$$

Finding analytic solution of (40) is not feasible. In general, it must be solved iteratively. The gradient of Ψ_L is:

$$\frac{\partial \Psi_L}{\partial f_{(j,l)}} = \sum_{i=1}^{N_i} \left[\frac{1}{2} \left(\frac{1}{\sigma_i^2} - g_i^2 \right) \frac{\partial \sigma_i^2}{\partial f_{(j,l)}} - g_i \frac{\partial \eta_i}{\partial f_{(j,l)}} - \hat{v} g_i \frac{1}{b_i^2} \frac{\partial b_i}{\partial f_{(j,l)}} \right] \quad (42)$$

$$\simeq \sum_{i=1}^{N_i} \left[\frac{1}{2} \left(\frac{1}{\sigma_i^2} - g_i^2 \right) \frac{\partial \sigma_i^2}{\partial f_{(j,l)}} - g_i \frac{\partial \eta_i}{\partial f_{(j,l)}} \right] \quad (43)$$

where g_i is defined as:

$$g_i = \frac{h_i - \eta_i + \hat{v}/b_i}{\sigma_i^2}. \quad (44)$$

To derive the approximated gradient (43) from the exact gradient (42), we need to check the order of each partial derivative term. One can verify that

$$\frac{1}{b_i^2} \frac{\partial b_i}{\partial f_{(j,l)}} \sim O(\mathcal{E}), \quad (45)$$

$$\frac{\partial \eta_i}{\partial f_{(j,l)}} \sim O(\mathcal{E}\mathcal{Y}), \quad (46)$$

$$\frac{\partial \sigma_i^2}{\partial f_{(j,l)}} \sim O(\mathcal{E}^2\mathcal{Y}), \quad (47)$$

where \mathcal{Y} is the dimension of the photon counts, and \mathcal{E} the energy level. Since $\mathcal{Y} \gg 1$, we can safely remove the partial derivative of b_i from (42). This approximation also applies to the preconditioner that is derived later. The remaining partial derivative

terms in (43) can be further expanded by finding the partial derivative of $\bar{y}_{(i,k)}$ with respect to $f_{(j,l)}$ as

$$\frac{\partial \bar{y}_{(i,k)}}{\partial f_{(j,l)}} = -I_{(i,k)}^0 u_{(k,l)} a_{(i,j)} \\ \exp \left(- \sum_{l=1}^{N_l} u_{(k,l)} [\mathbf{A}\mathbf{f}]_i \right) \\ = -a_{(i,j)} u_{(k,l)} \bar{y}_{(i,k)}, \quad (48)$$

$$\frac{\partial \eta_i}{\partial f_{(j,l)}} = \sum_{k=1}^{N_k} m_{E_k}^{(1)} \frac{\partial \bar{y}_{(i,k)}}{\partial f_{(j,l)}} \\ = -a_{(i,j)} \sum_{k=1}^{N_k} \left(u_{(k,l)} m_{E_k}^{(1)} \right) \bar{y}_{(i,k)}, \quad (49)$$

$$\frac{\partial \sigma_i^2}{\partial f_{(j,l)}} = \sum_{k=1}^{N_k} m_{E_k}^{(2)} \frac{\partial \bar{y}_{(i,k)}}{\partial f_{(j,l)}} \\ = -a_{(i,j)} \sum_{k=1}^{N_k} \left(u_{(k,l)} m_{E_k}^{(2)} \right) \bar{y}_{(i,k)}. \quad (50)$$

Substituting (49) and (50) into (43) yields

$$\frac{\partial \Psi_L}{\partial f_{(j,l)}} \simeq \sum_{i=1}^{N_i} a_{(i,j)} \left[\frac{1}{2} \left(\frac{1}{\sigma_i^2} - g_i^2 \right) n_{(i,l)}^{(2)} - g_i n_{(i,l)}^{(1)} \right], \quad (51)$$

where

$$n_{(i,l)}^{(1)} = - \sum_{k=1}^{N_k} u_{(k,l)} m_{E_k}^{(1)} \bar{y}_{(i,k)}, \quad (52)$$

$$n_{(i,l)}^{(2)} = - \sum_{k=1}^{N_k} u_{(k,l)} m_{E_k}^{(2)} \bar{y}_{(i,k)}. \quad (53)$$

D. Preconditioned Gradient Descent (Approximated Majorization-Minimization)

So far, we have obtained the data-fitting objective function (39) and its gradient (51) with respect to the parameters to be estimated, i.e., the fraction image of the l th material $f_{(j,l)}$. Using those equations, we want to find the minimum by taking the direction of the negative gradient. The preconditioned gradient descent method is:

$$\mathbf{f}^{(q+1)} = \mathbf{f}^{(q)} - \mathbf{N}_L^{-1} \nabla \Psi_L(\mathbf{f}^{(q)}). \quad (54)$$

Here, preconditioner \mathbf{N}_L defines the step size. Depending on the characteristics of the objective function, if the eigenvalues of \mathbf{N}_L^{-1} are too large, the iterates may not converge at all. On the other hand, if the eigenvalues of \mathbf{N}_L^{-1} are too small, convergence may be slow. Thus finding appropriate step size is crucial for fast and stable iterative computation.

Computing optimal \mathbf{N}_L for non-linear problems is challenging, and can be computationally expensive. In this case, a surrogate function $\Psi_L^{(q)}$ at each iteration step q can be adopted, which

is easier than the objective function to solve. Then, instead of minimizing the objective function, we minimize the surrogate function to move to the next iteration. This process is called majorization-minimization (MM) [44].

MM involves finding a majorizer $\Psi_L^{(q)}$ at each iteration step q that satisfies the following majorization conditions:

$$\Psi_L^{(q)}(\mathbf{f}) \geq \Psi_L(\mathbf{f}) \text{ for all } \mathbf{f}, \quad (55)$$

$$\Psi_L^{(q)}(\mathbf{f}) = \Psi_L(\mathbf{f}) \text{ for } \mathbf{f} = \mathbf{f}^{(q)}. \quad (56)$$

There are many majorization tricks that satisfy (55) and (56). Here, we use a separable quadratic surrogate based on a Hessian approximation. When $\mathbf{D}_L \succeq \mathcal{H}\Psi_L(\mathbf{f})$ for any \mathbf{f} , where $\mathcal{H}\{\cdot\}$ is the Hessian and \mathbf{D}_L is a diagonal matrix, then one can design a quadratic surrogate function that satisfies (55) and (56) as

$$\begin{aligned} \Psi_L(\mathbf{f}) &\leq \Psi_L^{(q)}(\mathbf{f}; \mathbf{f}^{(q)}) \\ &= \Psi_L(\mathbf{f}^{(q)}) + \nabla \Psi_L(\mathbf{f}^{(q)})' (\mathbf{f} - \mathbf{f}^{(q)}) \\ &\quad + \frac{1}{2} (\mathbf{f} - \mathbf{f}^{(q)})' \mathbf{D}_L (\mathbf{f} - \mathbf{f}^{(q)}). \end{aligned} \quad (57)$$

Then, the update finds the minimizer of $\Psi_L^{(q)}(\mathbf{f}; \mathbf{f}^{(q)})$:

$$\mathbf{f}^{(q+1)} = \arg \min_{\mathbf{f}} \Psi_L^{(q)}(\mathbf{f}; \mathbf{f}^{(q)}), \quad (58)$$

which leads to an update exactly of the form (54).

Designing $\Psi_L^{(q)}$ that satisfies (57) may lead to slow convergence. Instead, we find an approximate curvature that still typically decreases the objective function approximately monotonically.

We approximate the Hessian elements as:

$$\begin{aligned} \frac{\partial^2 \psi_{Li}}{\partial f_{(j_1, l_1)} \partial f_{(j_2, l_2)}} &\simeq \frac{1}{\sigma_i^2} \frac{\partial \eta_i}{\partial f_{(j_1, l_1)}} \frac{\partial \eta_i}{\partial f_{(j_2, l_2)}} \\ &+ \frac{g_i}{\sigma_i^2} \left(\frac{\partial \eta_i}{\partial f_{(j_1, l_1)}} \frac{\partial \sigma_i^2}{\partial f_{(j_2, l_2)}} + \frac{\partial \sigma_i^2}{\partial f_{(j_1, l_1)}} \frac{\partial \eta_i}{\partial f_{(j_2, l_2)}} \right) \\ &- g_i \frac{\partial^2 \eta_i}{\partial f_{(j_1, l_1)} \partial f_{(j_2, l_2)}} + \frac{g_i^2}{\sigma_i^2} \frac{\partial \sigma_i^2}{\partial f_{(j_1, l_1)}} \frac{\partial \sigma_i^2}{\partial f_{(j_2, l_2)}} \\ &- \frac{1}{2} g_i^2 \frac{\partial^2 \sigma_i^2}{\partial f_{(j_1, l_1)} \partial f_{(j_2, l_2)}}, \end{aligned} \quad (59)$$

where $\psi_{Li} = \psi_L(\bar{\mathbf{y}}_i)$. Expand all partial derivatives, and substitute:

$$\frac{\partial^2 \psi_{Li}}{\partial f_{(j_1, l_1)} \partial f_{(j_2, l_2)}} \simeq a_{(i, j_1)} a_{(i, j_2)} w_{(i, l_1, l_2)}, \quad (60)$$

where $w_{(i, l_1, l_2)}$ is defined as:

$$\begin{aligned} w_{(i, l_1, l_2)} &\equiv \left[\frac{1}{\sigma_i^2} n_{(i, l_1)}^{(1)} n_{(i, l_2)}^{(1)} \right. \\ &+ \frac{g_i}{\sigma_i^2} \left(n_{(i, l_1)}^{(1)} n_{(i, l_2)}^{(2)} + n_{(i, l_1)}^{(2)} n_{(i, l_2)}^{(1)} \right) - g_i n_{(i, l_1, l_2)}^{(1)} \\ &\left. + \frac{g_i^2}{\sigma_i^2} n_{(i, l_1)}^{(2)} n_{(i, l_2)}^{(2)} - \frac{g_i^2}{2} n_{(i, l_1, l_2)}^{(2)} \right], \end{aligned} \quad (61)$$

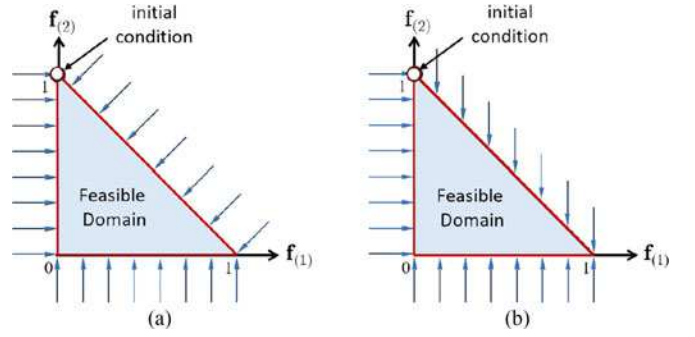


Fig. 7. Simplex projections; (a) to-the-closest-point, (b) two-direction.

where $n_{(i, l)}^{(1)}$ and $n_{(i, l)}^{(2)}$ are defined in (52) and (53) respectively. $n_{(i, l_1, l_2)}^{(1)}$ and $n_{(i, l_1, l_2)}^{(2)}$ are defined as:

$$n_{(i, l_1, l_2)}^{(1)} = \sum_{k=1}^{N_k} u_{(k, l_1)} u_{(k, l_2)} m_{E_k}^{(1)} \bar{y}_{(i, k)}, \quad (62)$$

$$n_{(i, l_1, l_2)}^{(2)} = \sum_{k=1}^{N_k} u_{(k, l_1)} u_{(k, l_2)} m_{E_k}^{(2)} \bar{y}_{(i, k)}. \quad (63)$$

The approximate Hessian based on the $w_{(i, l_1, l_2)}$ terms in (61) has coupling between the material fraction images. We first form a block diagonal majorizer for that Hessian that decouples those images, where the block corresponding to the l th material is:

$$\mathbf{N}_{L(l)}^{(q)} = \mathbf{A}' \mathbf{W}_{(l)}^{(q)} \mathbf{A}, \quad (64)$$

where $\mathbf{W}_{(l)}^{(q)} = \text{diag} \left[\sum_{l_2=1}^{N_{l_2}} |w_{(i, l_1, l_2)}^{(q)}| \right]_{i=1}^{N_i}$, $w_{(i, l_1, l_2)}^{(q)}$ denotes $w_{(i, l_1, l_2)}$ at q th iteration, and $\text{diag}[t_s]_{s=1}^N$ denotes a diagonal matrix with diagonal entries t_1, \dots, t_N . Most of the terms in (64) do not require additional computation as they are already found when computing the gradient, except $n_{(i, l_1, l_2)}^{(1)}$ and $n_{(i, l_1, l_2)}^{(2)}$. However, even this block diagonal majorizer would be too expensive to invert, so we use a diagonal majorizer (separable quadratic surrogate) [45], [46]:

$$\mathbf{D}_{L(l)}^{(q)} = \text{diag} \left[\mathbf{A}' \mathbf{W}_{(l)}^{(q)} \mathbf{A} \mathbf{1} \right], \quad (65)$$

where $\mathbf{1}$ is the all-ones vector and $\text{diag}[\mathbf{t}]$ denotes a diagonal matrix with diagonal entries being the elements of the vector \mathbf{t} . Forward-projection $\mathbf{A} \mathbf{1}$ can be pre-computed, thus additional overhead required at each step is mostly a single back-projection. The supplement provides a detailed derivation of the majorizers (64) and (65).

The iteration (54) needs to consider the non-negative and volume-fraction-sum constraints \mathcal{F} , where the set \mathcal{F} is defined in (41). For the case of dual material decomposition, the feasible domain that satisfies (41) forms a triangle in two dimensional plane. In general, the projection onto the simplex moves the exterior points to the closest points on the simplex, which usually involves orthogonal projection as shown in Fig. 7(a). However, quite often, the direction of the gradient vector normalized by the approximated Hessian is nearly orthogonal to the hypotenuse due to the ill-posed nature of the problem. In that case, the orthogonal projection nearly cancels out the update.

The supplement provides a one-dimensional example when the projection-to-the-closest point fails. Instead, we used the following two-direction projection scheme:

$$\mathbf{f}_{(1)}^{(q+1)} = \mathcal{P}_1 \left[\mathbf{f}_{(1)}^{(q)} - \mathbf{M} \left(\mathbf{D}_{L(1)}^{(q)} \right)^{-1} \nabla_{\mathbf{f}_{(1)}} \Psi_L^{(q)} \right], \quad (66)$$

$$\mathbf{f}_{(2)}^{(q+1)} = \mathcal{P}_2 \left[\mathbf{f}_{(2)}^{(q)} - \mathbf{M} \left(\mathbf{D}_{L(2)}^{(q)} \right)^{-1} \nabla_{\mathbf{f}_{(2)}} \Psi_L^{(q)}; \mathbf{f}_{(1)}^{(q+1)} \right], \quad (67)$$

where $\mathcal{P}_1[t]$ and $\mathcal{P}_2[t; s]$ are element-wise projection operators defined as:

$$\mathcal{P}_1[t] = \min [\max [t, 0], 1], \quad (68)$$

$$\mathcal{P}_2[t; s] = \min [\max [t, 0], 1 - s], \quad (69)$$

and \mathbf{M} is the masking matrix. Fig. 7(b) shows the graphical representation of the two-direction projection. This approximated projection requires a specific setting: the material corresponding to $\mathbf{f}_{(1)}$ needs to have higher attenuation coefficients than the other. As a material fraction image with higher attenuation converges faster, a lower attenuation material fraction image can take the advantage of the faster converging higher attenuation material image. The masking matrix \mathbf{M} in (66) and (67) is essential for minimizing limited angle artifacts due to the lack of information by multiplying zeros to pixels outside the ‘known outline’ of the object:

$$\begin{aligned} \mathbf{M} &= \text{diag}[m_j]_{j=1}^{N_j}, \\ m_j &= \mathbb{1}\{j \in \mathbb{Q}\}, \end{aligned} \quad (70)$$

where $\mathbb{1}\{t\}$ is the indicator function, 1 if t is true and 0 otherwise. \mathbb{Q} is the known bounded domain in the image where no objects are located outside of it.

E. Regularizer

To help ensure a unique solution for this ill-posed problem, we include a regularizer. An objective function with a regularizer can be written in an additive form as

$$\hat{\mathbf{f}} = \arg \min_{\mathbf{f} \in \mathbb{F}} \{ \Psi_L(\mathbf{f}) + \kappa \Psi_R(\mathbf{f}) \}, \quad (71)$$

where κ denotes a regularization parameter. Regularization term Ψ_R does not have to be the same for every material fraction image $\mathbf{f}_{(l)}$. Different regularizers can be applied depending on the characteristics of the objects in the fraction images. A hard material (metal) fraction image generally has flatter and sharper-edged objects than a soft material (liquid) fraction image. By experiments, we found that a combination of an edge-preserving hyperbolic regularizer and a sparsity-based ℓ_0 -norm regularizer can effectively remove the limited angle artifacts in the hard material fraction image, while applying only the edge-preserving hyperbolic regularizer to the soft material fraction image. The objective function is:

$$\hat{\mathbf{f}} = \arg \min_{\mathbf{f} \in \mathbb{F}} \left\{ \Psi_L(\mathbf{f}) + \sum_l \kappa_{(l)} \Psi_R(\mathbf{f}_{(l)}) + \kappa_0 \|\mathbf{f}_{(1)}\|_0 \right\}, \quad (72)$$

where $\|\mathbf{t}\|_0$ is defined as

$$\|\mathbf{t}\|_0 = \sum_j \mathbb{1}\{t_j \neq 0\}. \quad (73)$$

$\Psi_R(\cdot)$ is the edge-preserving hyperbola regularizer defined as

$$\Psi_R(\mathbf{f}_{(l)}) = \sum_{p=1}^{N_p} \psi_R(\mathbf{C}\mathbf{f}_{(l)}), \quad (74)$$

where \mathbf{C} is the first-order finite difference matrix, and $\psi_R(t)$ is an element-wise scalar hyperbola function defined as

$$\psi_R(t) = \delta_R^2 \left(\sqrt{1 + (t/\delta_R)^2} - 1 \right). \quad (75)$$

To solve (72), we first need to obtain the gradient descent solution of the differentiable part, excluding the ℓ_0 norm regularization. A separable preconditioner for the differentiable regularization term can be found from the spectral radius of the Hessian matrix. Since the curvature of the hyperbola potential is bounded, i.e., $\ddot{\psi}_R \leq 1$,

$$\begin{aligned} \mathcal{H}\Psi_{R(l)} &= \mathbf{C}' \text{diag} \left[\ddot{\psi}_R([\mathbf{C}\mathbf{f}_{(l)}]_p) \right] \mathbf{C} \\ &\succeq \mathbf{C}' \mathbf{I} \mathbf{C} \succeq \mathbf{D}_R \equiv c_R \mathbf{I}, \end{aligned} \quad (76)$$

where c_R is the spectral radius of the matrix $\mathbf{C}'\mathbf{C}$. For 2-D problem, using horizontal and vertical neighbors, c_R can be found as

$$c_R = \max(|\mathcal{F}\{\mathbf{C}'_x \mathbf{C}_x\}|) + \max(|\mathcal{F}\{\mathbf{C}'_y \mathbf{C}_y\}|) = 8, \quad (77)$$

where $\mathcal{F}\{\mathbf{A}\}$ is the 1-D discrete Fourier transform operator taking the first row of \mathbf{A} as an input. Finally, the transition equation for the preconditioned gradient descent in (66) and (67) can be rewritten after including the regularization terms as

$$\begin{aligned} \mathbf{f}_{(l)}^{(q+1)} &= \mathcal{P}_l \left[\mathbf{f}_{(l)}^{(q)} - \mathbf{M} \left(\mathbf{D}_{(l)}^{(q)} \right)^{-1} \nabla_{\mathbf{f}_{(l)}} \Psi^{(q)} \right] \\ &= \mathcal{P}_l \left[\mathbf{f}_{(l)}^{(q)} - \mathbf{M} \left(\mathbf{D}_{L(l)}^{(q)} + \kappa_{(l)} \mathbf{D}_{R(l)} \right)^{-1} \right. \\ &\quad \left. \cdot \left(\nabla_{\mathbf{f}_{(l)}} \Psi_L^{(q)} + \kappa_{(l)} \nabla_{\mathbf{f}_{(l)}} \Psi_{R(l)}^{(q)} \right) \right]. \end{aligned} \quad (78)$$

The overall objective function (72) including the sparsity based regularizer can be solved using the iterative shrinkage-thresholding algorithm (ISTA), which is a proximal gradient (PG) method [47]. ISTA is an extension of the gradient descent method, where a shrinkage operator is iteratively applied after taking the gradient descent step without the sparsity regularizer. For ℓ_0 norms, the corresponding proximal operator is the element-wise hard-thresholding shrinkage operator, defined as

$$\mathcal{T}[t; s] = t \cdot \mathbb{1}\{|t| > s\}. \quad (79)$$

Then, (72) can be solved by taking the following iterative step:

$$\mathbf{f}_{(1)}^{(q+1)} = \mathcal{T} \left[\mathcal{P}_1 \left[\mathbf{f}_{(1)}^{(q)} - \mathbf{M} \left(\mathbf{D}_{(1)}^{(q)} \right)^{-1} \nabla_{\mathbf{f}_{(1)}} \Psi^{(q)} \right] \right]. \quad (80)$$

Note that ℓ_0 norm regularizer is applied only to the hard material fraction image $l = 1$, so there is no change for $l = 2$. (80) can

Algorithm 1: Adaptive restart GAPG.

```

1:  $\mathbf{z}_{(1)}^{(0)} = \mathbf{f}_{(1)}^{(0)}, \mathbf{z}_{(2)}^{(0)} = \mathbf{f}_{(2)}^{(0)}, d^{(0)} = 1$ 
2: for  $q = 0, 1, \dots$  do
3:    $\mathbf{z}^{(q)} = [\mathbf{z}_{(1)}^{(q)}, \mathbf{z}_{(2)}^{(q)}]$ 
4:    $\mathbf{f}_{(1)}^{(q+1)} = \mathcal{Q} \left[ \mathbf{z}_{(1)}^{(q)} - \mathbf{M} \left( \mathbf{D}_{(1)}^{(q)} \right)^{-1} \nabla_{\mathbf{f}_{(1)}} \Psi \left( \mathbf{z}^{(q)} \right) \right. \\ \left. ; \kappa_0 \left( \mathbf{D}_{(1)}^{(q)} \right)^{-1} \mathbf{1} \right]$ 
5:    $\mathbf{f}_{(2)}^{(q+1)} = \mathcal{P}_2 \left[ \mathbf{z}_{(2)}^{(q)} - \mathbf{M} \left( \mathbf{D}_{(2)}^{(q)} \right)^{-1} \nabla_{\mathbf{f}_{(2)}} \Psi \left( \mathbf{z}^{(q)} \right) \right. \\ \left. ; \mathbf{z}_{(1)}^{(q)} \right]$ 
6:   if  $\sum_l (\nabla_{\mathbf{f}_{(l)}} \Psi)'(\mathbf{f}_{(l)}^{(q+1)} - \mathbf{f}_{(l)}^{(q)}) > 0$  then
7:      $d^{(q)} = 1$ 
8:   end if
9:    $d^{(q+1)} = (1 + \sqrt{1 + 4(d^{(q)})^2})/2$ 
10:   $\mathbf{z}_{(1)}^{(q+1)} = \mathbf{f}_{(1)}^{(q+1)} + \frac{d^{(q)} - 1}{d^{(q+1)}} (\mathbf{f}_{(1)}^{(q+1)} - \mathbf{f}_{(1)}^{(q)})$ 
11:   $\mathbf{z}_{(2)}^{(q+1)} = \mathbf{f}_{(2)}^{(q+1)} + \frac{d^{(q)} - 1}{d^{(q+1)}} (\mathbf{f}_{(2)}^{(q+1)} - \mathbf{f}_{(2)}^{(q)})$ 
12:   $q = q + 1$ 
13: end for

```

be further simplified by merging the hard-thresholding operator $\mathcal{T}[\cdot]$ and the projection operator $\mathcal{P}_1[\cdot]$, which becomes the truncated hard-thresholding operator:

$$\mathbf{f}_{(1)}^{(q+1)} = \mathcal{Q} \left[\mathbf{f}_{(1)}^{(q)} - \mathbf{M} \left(\mathbf{D}_{(1)}^{(q)} \right)^{-1} \nabla_{\mathbf{f}_{(1)}} \Psi^{(q)}; \kappa_0 \left(\mathbf{D}_{(1)}^{(q)} \right)^{-1} \mathbf{1} \right], \quad (81)$$

where the element-wise operator $\mathcal{Q}[t; s]$ is defined as

$$\mathcal{Q}[t; s] = \begin{cases} 0 & \text{if } t < s \\ t & \text{if } s \leq t < 1 \\ 1 & \text{if } t \geq 1 \end{cases}. \quad (82)$$

While ISTA can be applied to the gradient method without much effort, the convergence speed of ISTA is slow. To accelerate the convergence of the proximal gradient method, Nesterov's momentum-based method is widely used because of its simplicity. Beck and Teboulle [48] introduced a fast iterative shrinkage-thresholding algorithm (FISTA) that has a convergence rate $O(1/q^2)$ using the Nesterov's linear momentum acceleration method [49]. While the original FISTA algorithm is designed for the Lipschitz continuous function, Zuo and Lin [50] further generalized the algorithm to the quadratic, preferably separable, surrogate problem that leads to the faster convergence, called the generalized accelerated proximal gradient method (GAPG). Nesterov's momentum method can lead to overshoot; O'Donoghue and Candès [51] suggested a gradient-based restart approach to avoid the overshoot. We combined the gradient-based restart scheme with GAPG as an acceleration method in this study, summarized in Algorithm 1.

IV. SIMULATION RESULT

We performed simulations to assess the effectiveness of the proposed method, and compared the result with the existing simple Poisson (SP) method suggested by Lasio *et al.* [38]. SP converts energy-integrated data into photon-counting-equivalent data by dividing it by mean energy, and then uses single material approximation to avoid the ill-posedness. In Lasio *et al.*, the exact mean energy after attenuation is used to get the photon-counting-equivalent data by assuming all location and attenuation properties of high density objects are perfectly known beforehand. Here, we did not apply this mean energy correction for the SP results as we assume that the location of metal objects are unknown.

We considered three different cases; SP, NGA with volume-fraction-sum constraints, and NGA without volume-fraction-sum constraints; and three different source settings; 5 kW, 20 kW, and noiseless. Minimum and maximum photons/detector for 5 kW source were 9 and 140, respectively, while those for 20 kW source were 39 and 500. All other simulation conditions for the source and detectors are identical with the system specification shown in Table I, and the graphical representation of the system geometry shown in Fig. 2.

We neglect readout noises, charge sharing between neighboring detectors and scattering of X-ray photons in the simulation. We assume the electron beam is ideally pulsed and focused, i.e., the focal spot area of the electron beam is infinitesimal, and the source location at each projection is not moving during data acquisition. (Here, we neglect the effect of charge sharing, scattering, and finite focal spot to focus on the specific problem such as beam hardening and limited angle artifacts. Depending on the system, image blurring due to those factors can significantly degrade the result.)

We obtained the initial spectrum using the numerical simulation program 'SpekCalc v1.1' [52] with 5 mm aluminum filter. SpekCalc returns photon flux measured 1 m away from the source with the right impinging angle. We modulated the initial spectrum for each ray to consider the effect of the distance and impinging angle using the following equation:

$$I_{(i,k)}^0 = I_{(k)}^S A_d \left(\frac{1}{d_{(i)}} \right)^2 \cos(a_{(i)}), \quad (83)$$

where $I_{(i,k)}^0$ is the corrected initial emission spectrum of the i th ray at k th energy level, $I_{(k)}^S$ is the initial emission spectrum obtained by SpekCalc software at k th energy level, A_d is the detector face area in cm^2 , $d_{(i)}$ is the distance between the source and detector in m, and $a_{(i)}$ is the impinging angle of the i th ray.

We obtained attenuation coefficients by interpolating the attenuation coefficient tables of NIST [53]. Assuming the pipe location is known, we initialized volume fraction images as a fully water-filled pipe, i.e., set the true image of the pipe as the initial condition of the titanium volume fraction, and the initial water volume fraction as one inside the pipe, and zero otherwise. We applied noise on the sinogram in accordance with the shifted gamma distribution using the parameters shown in (25), (26), and (27).

TABLE II
ROOT MEAN SQUARED ERRORS OF THE WATER REGIONS (RMSE_w) FOR
THREE DIFFERENT RECONSTRUCTION METHODS

Method	5 kW	20 kW	Noiseless
SP	0.331	0.302	0.293
NGA without VFSC ¹	0.142	0.106	0.097
NGA with VFSC	0.117	0.096	0.092

¹volume-fraction-sum constraints.

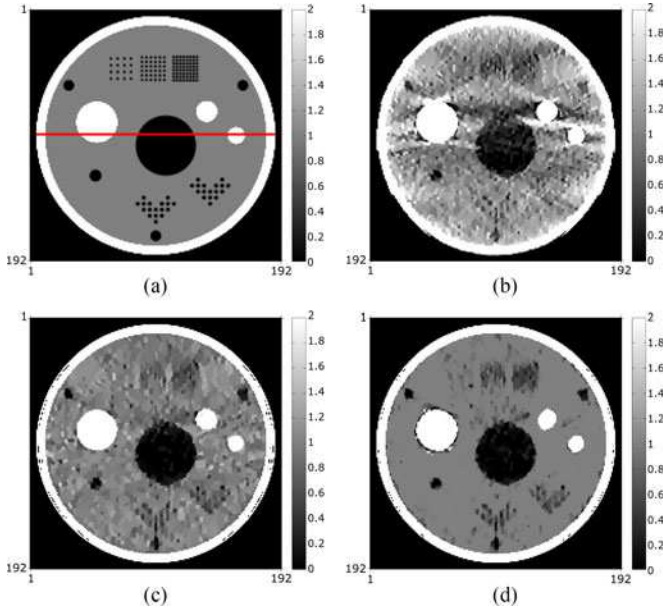


Fig. 8. Comparison of reconstruction results with 150 kV, 5 kW source for three different methods; (a) true image, (b) SP, (c) NGA without volume-fraction-sum constraints, (d) NGA with volume-fraction-sum constraints. The red line on (a) is the sampled location of the profiles for comparison shown in Fig. 9.

We set the shape parameter δ_R of the hyperbola potential regularizer to be 0.005 for both the titanium and water volume fraction images throughout every simulation. The effectiveness of the regularization parameter for the water image $\kappa_{(2)}$ can be different for SP and NGA models, and it depends on the units of the data-fitting objective functions. Following Fessler and Rogers [54], we match the regularization parameters to have the same response of the single pixel local impulse at the center of the image for SP and NGA models. Based on the local impulse resolution test with 2 kW source (equivalent to 20 kW source with pipe), matching $\kappa_{(2)}$ for SP is approximately 3200 when regularization parameter for NGA is 3000. The supplement provides local impulse responses for regularized SP and NGA with 2 kW source. For 5 kW source, we scaled down $\kappa_{(2)}$ linearly to match the resolution, 750 for NGA and 800 for SP. For the NGA model, the regularizer for the titanium image is different from that of the water image, and we set κ_0 and $\kappa_{(1)}$ to be 2000 and 7000 for 20 kW source, and 500 and 1750 for 5 kW source, respectively. This material-specific regularization requires a material decomposition, thus it cannot be applied to SP.

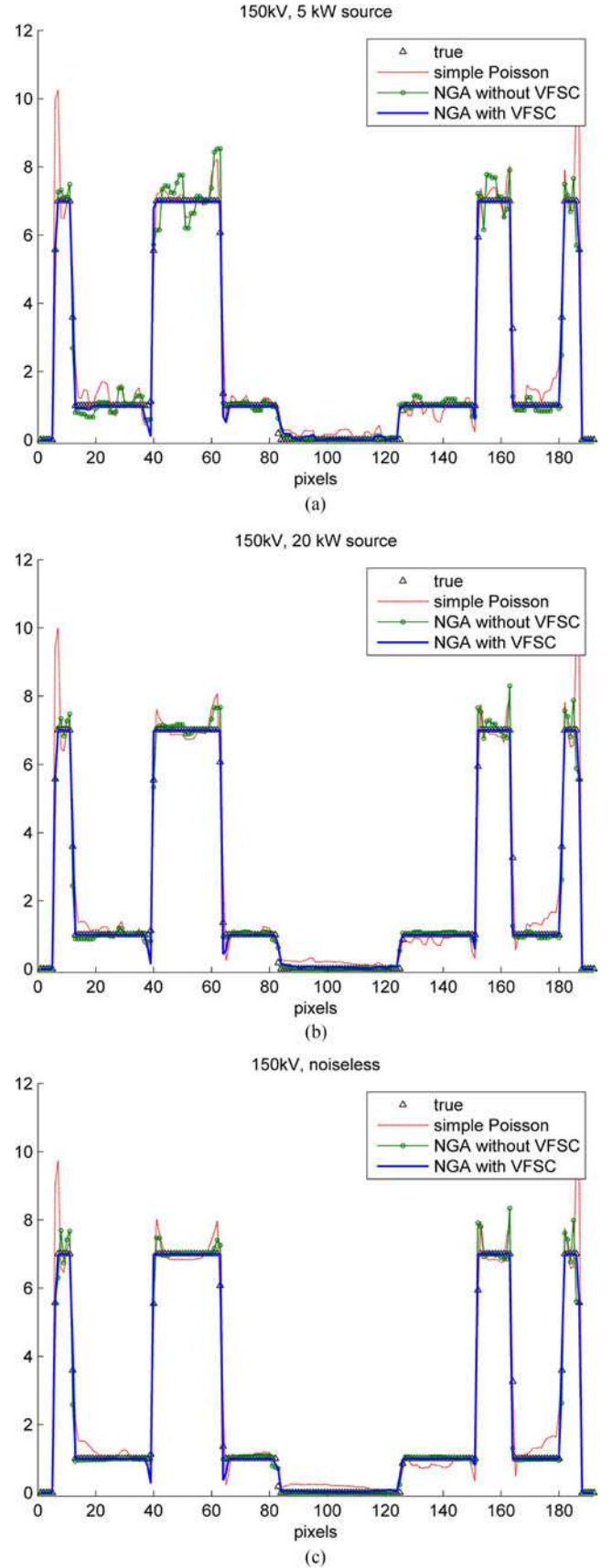


Fig. 9. Comparisons of profiles for three different source power settings; (a) 5 kW, (b) 20 kW, (c) noiseless. The location of the sampled profile is shown in Fig. 8(a).

To compare the quality of images between SP and NGA, we first merge the dual material volume fraction maps of NGA into a single equivalent density image:

$$\mathbf{f} = 7\mathbf{f}_{(1)} + \mathbf{f}_{(2)}, \quad (84)$$

where the factor 7 is a rough estimation of the equivalent density of titanium based on the SP results. Because the true value of the titanium in SP is unknown as it is based on the single material (water) assumption, we only consider the root mean square errors (RMSE) of the water region. To compute water-only RMSE (RMSE_w), we removed the region where the titanium volume fraction is higher than 0.01 from the image for both the SP and NGA results:

$$\text{RMSE}_w = \sqrt{1/N_j \sum_j (\hat{f}_{(j,2)} - \bar{f}_{(j,2)})^2}. \quad (85)$$

Table II shows RMSE_w results of three different methods when the source is set 5 kW, 20 kW, and noiseless. Fig. 8 shows the results of three different methods with 5 kW source. Fig. 9 shows the comparisons of the center profiles for three different methods.

In summary, NGA with volume-fraction-sum constraints gives the best results throughout all the source settings considered. CT reconstructions based on the limited angle data typically have crisscross patterned artifacts near the tip of each object, showing the lack of projection data tangential to the outline. Those patterns can be seen on the SP result in Fig. 8(b), but significantly reduced in Fig. 8(c) and (d). Without volume-fraction-sum constraints, NGA still reduces cupping artifacts due to the beam-hardening when compared to SP, as can be seen from noiseless results in Fig. 9(c). At 20 kW, NGA without volume-fraction-sum constraints outperforms SP everywhere. At 5 kW, NGA without volume-sum-fraction constraints still works better at the water region, but getting more noise at the tungsten region, where photons/detector becomes extremely low; minimum of 9 photons/detector. It is seemingly due to the Gaussian approximation deviating from the original skewed Compound Poisson distribution.

V. CONCLUSION

We proposed a CT reconstruction method for a limited angle, single bin energy integrating measurement CT system. For the data-fitting term, the method involved a nonlinear Gaussian approximation (NGA) model for the energy-integrating statistics combined with the volume fraction material decomposition method. NGA model can reduce the beam-hardening artifacts and noise, except in the case when the photon flux is extremely low. The volume-fraction-sum constraints confine the iterative solution to be close to the true solution to help solve the original ill-posed problem, and they are shown to be effective not only to separate the volume fraction for each material, but also to reduce the beam-hardening and limited angle artifacts.

We applied ℓ_0 norm and edge-preserving hyperbola regularizers accordingly depending on the characteristics of materials.

The role of regularizers was to provide additional removal of small local volume fraction errors and limited angle artifacts.

We used an approximate Hessian along with the separable quadratic surrogate functions to simplify the minimization step while maintaining a reasonable convergence speed. The method has not been proven to monotonically decrease the objective function for all cases, thus a further study regarding the convergence may be required in the future.

The regularizers we utilized had many parameters to be tuned, as two regularization schemes are combined. The ℓ_0 norm and edge-preserving hyperbola potential regularizer are connected by the curvature, and competing with each other. Actual strength of the ℓ_0 norm regularizer depends on the strength parameter of the edge-preserving regularizer indirectly, as well as its own strength parameter. Finding optimal values for the strength parameters may require combining the strength parameters into a single parameter.

Throughout the simulation, we made several assumptions that may affect the quality of the result in practice. Those include no charge sharing, no scattering of X-ray photons, no readout noise, and ideally pulsed and focused electron beam. Evaluating the algorithm with real data will be performed in the future, once the proposed CT system is fully operational.

REFERENCES

- [1] M. Bieberle and U. Hampel, "Evaluation of a limited angle scanned electron beam x-ray CT approach for two-phase pipe flows," *Meas. Sci. Technol.*, vol. 17, no. 8, pp. 2057–2065, 2006.
- [2] F. Fischer *et al.*, "An ultra fast electron beam x-ray tomography scanner," *Meas. Sci. Technol.*, vol. 19, p. 094002, 2008.
- [3] R. F. Mudde, "Time-resolved X-ray tomography of a fluidized bed," *Powder Technol.*, vol. 199, no. 1, pp. 55–59, 2010.
- [4] T. J. Heindel, "A review of X-ray flow visualization with applications to multiphase flows," *J. Fluids Eng.*, vol. 133, no. 7, p. 74001, 2011.
- [5] T. Stürzel *et al.*, "Experimental facility for two- and three-dimensional ultrafast electron beam x-ray computed tomography," *Rev. Sci. Instrum.*, vol. 82, no. 2, p. 023702, 2011.
- [6] U. Hampel, F. Barthel, M. Bieberle, and T. Strzel, "Transparent target for ultrafast electron beam tomography," *Nucl. Instrum. Methods Phys. Res. Sec. A, Accelerators, Spectrometers, Detectors Associated Equip.*, vol. 635, no. 1, pp. 8–12, 2011.
- [7] M. Bieberle, F. Barthel, and U. Hampel, "Ultrafast X-ray computed tomography for the analysis of gas-solid fluidized beds," *Chem. Eng. J.*, vol. 189–190, pp. 356–363, 2012.
- [8] U. Hampel, F. Barthel, M. Bieberle, M. Schubert, and E. Schleicher, "Multiphase flow investigations with ultrafast electron beam x-ray tomography," *AIP Conf. Proc.*, vol. 167, pp. 167–174, 2012.
- [9] S. A. Mäkiharju, "The dynamics of ventilated partial cavities over a wide range of Reynolds numbers and quantitative two-dimensional X-ray densitometry for multiphase flow," Ph.D. dissertation, Univ. Michigan, Ann Arbor, MI, USA, 2012.
- [10] S. A. Mäkiharju, C. Gabillet, B.-G. Paik, N. A. Chang, M. Perlin, and S. L. Ceccio, "Time-resolved two-dimensional X-ray densitometry of a two-phase flow downstream of a ventilated cavity," *Exp. Fluids*, vol. 54, no. 7, pp. 1–21, 2013.
- [11] M. Bieberle and U. Hampel, "Level-set reconstruction algorithm for ultrafast limited-angle X-ray computed tomography of two-phase flows," *Philos. Trans. Roy. Soc. London A, Math. Phys. Eng. Sci.*, vol. 373, no. 2043, 2015.
- [12] C. Brennen, *Fundamentals of Multiphase Flows*, vol. 128. Cambridge, U.K.: Cambridge Univ. Press, 2005.
- [13] A. Macovski, R. E. Alvarez, J. L. H. Chan, J. P. Stonestrom, and L. M. Zatz, "Energy dependent reconstruction in X-ray computerized tomography," *Comput. Biol. Med.*, vol. 6, no. 4, pp. 325–336, 1976.

- [14] P. M. Joseph and R. D. Spital, "A method for correcting bone induced artifacts in computed tomography scanners," *J. Comput. Assist. Tomogr.*, vol. 2, no. 1, pp. 100–108, 1978.
- [15] W. H. Marshall, R. E. Alvarez, and A. Macovski, "Initial results with pre-reconstruction dual-energy computed tomography (PREDECT)," *Radiology*, vol. 140, no. 2, pp. 421–430, 1981.
- [16] J. P. Stonestrom, R. E. Alvarez, and A. Macovski, "A Framework for Spectral Artifact Corrections in X-Ray CT," *IEEE Trans. Biomed. Eng.*, vol. BME-28, no. 2, pp. 128–141, Feb. 1981.
- [17] N. Clinthorne, "A constrained dual-energy reconstruction method for material-selective transmission tomography," *Nucl. Instrum. Methods Phys. Res.*, vol. 353, no. 1–3, pp. 347–348, 1994.
- [18] S. Gleason and H. Sari-Sarraf, "Reconstruction of multi-energy x-ray computed tomography images of laboratory mice," *IEEE Trans. Nucl. Sci.*, vol. 46, no. 4, pp. 1081–1086, Aug. 1999.
- [19] P. Sukovic and N. Clinthorne, "Basis material decomposition using triple-energy X-ray computed tomography," in *Proc. IEEE 16th Instrum. Meas. Technol. Conf.*, 1999, pp. 1615–1618.
- [20] P. Sukovic and N. H. Clinthorne, "Penalized weighted least-squares image reconstruction for dual energy X-ray transmission tomography," *IEEE Trans. Med. Imag.*, vol. 19, no. 11, pp. 1075–1081, Nov. 2000.
- [21] C. H. Yan, R. T. Whalen, G. S. Beaupré, S. Y. Yen, and S. Napel, "Reconstruction algorithm for polychromatic CT imaging: Application to beam hardening correction," *IEEE Trans. Med. Imag.*, vol. 19, no. 1, pp. 1–11, Jan. 2000.
- [22] B. De Man, J. Nuyts, P. Dupont, G. Marchal, and P. Suetens, "An iterative maximum-likelihood polychromatic algorithm for CT," *IEEE Trans. Med. Imag.*, vol. 20, no. 10, pp. 999–1008, Oct. 2001.
- [23] I. A. Elbakri and J. A. Fessler, "Statistical image reconstruction for polyenergetic X-ray computed tomography," *IEEE Trans. Med. Imag.*, vol. 21, no. 2, pp. 89–99, Feb. 2002.
- [24] I. A. Elbakri and J. A. Fessler, "Efficient and accurate likelihood for iterative image reconstruction in X-ray computed tomography," *Proc. SPIE*, vol. 5032, pp. 1839–1850, 2003.
- [25] I. A. Elbakri and J. A. Fessler, "Segmentation-free statistical image reconstruction for polyenergetic x-ray computed tomography with experimental validation," *Phys. Med. Biol.*, vol. 48, no. 15, p. 2453, 2003.
- [26] P. E. Kinahan, A. M. Alessio, and J. A. Fessler, "Dual energy CT attenuation correction methods for quantitative assessment of response to cancer therapy with PET/CT imaging," *Technol. Cancer Res. Treatment*, vol. 5, no. 4, pp. 319–327, 2006.
- [27] L. P. Nogueira *et al.*, "Mapping lead distribution in bones by dual-energy computed microtomography with synchrotron radiation," *Proc. IEEE Nucl. Sci. Symp. Conf. Rec.*, 2009, pp. 3471–3474.
- [28] W. Huh and J. A. Fessler, "Model-based image reconstruction for dual-energy x-ray CT with fast KVP switching," in *Proc. IEEE Int. Symp. Biomed. Imag. Nano Macro*, 2009, pp. 326–329.
- [29] L. Yu, X. Liu, and C. H. McCollough, "Pre-reconstruction three-material decomposition in dual-energy CT," *Proc. SPIE*, vol. 7258, no. 8, 2009, p. 72583V, 2009.
- [30] C. Maaß, R. Grimmer, and M. Kachelrieß, "Dual energy CT material decomposition from inconsistent rays (MDIR)," in *Proc. IEEE Nucl. Sci. Symp. Conf. Rec.*, 2009, vol. 1, no. 1, pp. 3446–3452.
- [31] X. Liu, L. Yu, A. N. Primak, and C. H. McCollough, "Quantitative imaging of element composition and mass fraction using dual-energy CT: three-material decomposition," *Med. Phys.*, vol. 36, no. 5, pp. 1602–1609, 2009.
- [32] J. Noh, J. A. Fessler, and P. E. Kinahan, "Statistical sinogram restoration in dual-energy CT for PET attenuation correction," *IEEE Trans. Med. Imag.*, vol. 28, no. 11, pp. 1688–1702, Nov. 2009.
- [33] C. Cai, T. Rodet, S. Legoupil, and A. Mohammad-Djafari, "A full-spectral Bayesian reconstruction approach based on the material decomposition model applied in dual-energy computed tomography," *Med. Phys.*, vol. 40, no. 11, p. 111916, 2013.
- [34] C. O. Schirra *et al.*, "Statistical reconstruction of material decomposed data in spectral CT," *IEEE Trans. Med. Imag.*, vol. 32, no. 7, pp. 1249–1257, Jul. 2013.
- [35] Y. Long and J. Fessler, "Multi-material decomposition using statistical image reconstruction for spectral CT," *IEEE Trans. Med. Imag.*, vol. 33, no. 8, pp. 1614–1626, Aug. 2014.
- [36] R. Carmi, G. Naveh, and A. Altman, "Material separation with dual-layer CT," in *Proc. IEEE Nucl. Sci. Symp. Conf. Rec.*, 2005, vol. 4, pp. 1876–1878.
- [37] B. R. Whiting, P. Massoumzadeh, O. A. Earl, J. A. O'Sullivan, D. L. Snyder, and J. F. Williamson, "Properties of preprocessed sinogram data in x-ray computed tomography," *Med. Phys.*, vol. 33, no. 9, pp. 3290–3303, 2006.
- [38] G. M. Lasio, B. R. Whiting, and J. F. Williamson, "Statistical reconstruction for x-ray computed tomography using energy-integrating detectors," *Phys. Med. Biol.*, vol. 52, no. 8, pp. 2247–2266, 2007.
- [39] S. Srivastava, J. Cammin, G. S. K. Fung, B. M. W. Tsui, and K. Taguchi, "Spectral response compensation for photon-counting clinical x-ray CT using sinogram restoration," *Proc. SPIE*, vol. 8313, no. 410, pp. 831 311–1–831 311-7, 2012.
- [40] C. D. Daykin, T. Pentikainen, and M. Pesonen, *Practical Risk Theory for Actuaries*. Boca Raton, FL, USA: CRC Press, 1993.
- [41] H. Cramér, *Collective Risk Theory: A Survey of the Theory From the Point of View of the Theory of Stochastic Processes*. Nordiska bokhandeln, Stockholm, 1955.
- [42] R. Seri and C. Choirat, "Comparison of approximations for compound Poisson processes," *ASTIN Bull.*, vol. 45, no. 3, pp. 601–637, 2015.
- [43] R. Redus, "Efficiency and attenuation in CdTe detectors," Amptek Inc., Bedford, MA, USA, Application Note AN-CdTe-001, 2010.
- [44] J. M. Ortega and W. C. Rheinboldt, *Iterative Solution of Nonlinear Equations in Several Variables*, vol. 30. Philadelphia, PA, USA: SIAM, 1970.
- [45] J. Fessler, E. P. Ficaro, N. H. Clinthorne, and K. Lange, "Grouped-coordinate ascent algorithms for penalized-likelihood transmission image reconstruction," *IEEE Trans. Med. Imag.*, vol. 16, no. 2, pp. 166–175, Apr. 1997.
- [46] H. Erdogan and J. A. Fessler, "Ordered subsets algorithms for transmission tomography," *Phys. Med. Biol.*, vol. 44, no. 11, p. 2835, 1999.
- [47] A. Beck and M. Teboulle, "Gradient-based algorithms with applications to signal recovery," in *Convex Optimization in Signal Processing and Communications*. Cambridge, U.K.: Cambridge Univ. Press, 2009, pp. 42–88.
- [48] A. Beck and M. Teboulle, "A fast iterative shrinkage-thresholding algorithm for linear inverse problems," *SIAM J. Imag. Sci.*, vol. 2, no. 1, pp. 183–202, 2009.
- [49] Y. Nesterov, "A method of solving a convex programming problem with convergence rate $O(1/k^2)$," *Soviet Math. Doklady*, vol. 27, no. 2, pp. 372–376, 1983.
- [50] W. Zuo and Z. Lin, "A generalized accelerated proximal gradient approach for total-variation-based image restoration," *IEEE Trans. Image Process.*, vol. 20, no. 10, pp. 2748–2759, Oct. 2011.
- [51] B. O'Donoghue and E. Candès, "Adaptive restart for accelerated gradient schemes," *Found. Comput. Math.*, vol. 15, no. 3, pp. 715–732, Feb. 2013.
- [52] G. Poludniowski, G. Landry, F. DeBlois, P. M. Evans, and F. Verhaegen, "SpekCalc: A program to calculate photon spectra from tungsten anode x-ray tubes," *Phys. Med. Biol.*, vol. 54, no. 19, p. N433, 2009.
- [53] J. H. Hubbell and S. M. Seltzer, "Tables of X-ray mass attenuation coefficients and mass energy-absorption coefficients 1 keV to 20 MeV for elements $Z = 1$ to 92 and 48 additional substances of dosimetric interest," National Institute of Standards and Technology, Tech. Rep. NISTIR 5632, 1995.
- [54] J. A. Fessler and W. L. Rogers, "Spatial resolution properties of penalized-likelihood image reconstruction: Space-invariant tomographs," *IEEE Trans. Image Process.*, vol. 5, no. 9, pp. 1346–1358, Sep. 1996.

Image Reconstruction for Limited Angle Electron Beam X-Ray Computed Tomography with Energy-Integrating Detectors for Multiphase Flows: Supplementary Material

Seongjin Yoon, Simo A. Mäkiharju, Jeffrey A. Fessler, *Fellow, IEEE*, and Steven L. Ceccio

This supplementary material contains the geometry of the synthetic phantom used for simulations in [1], a derivation of the diagonal majorizer for the data-fitting objective function, a comparison of two simplex projection schemes in one-dimensional problem, and local impulse responses of regularized simple Poisson (SP) and nonlinear Gaussian approximation (NGA).

S1. GEOMETRY OF THE SYNTHETIC PHANTOM USED FOR SIMULATIONS IN [1]

The synthetic phantom is filled with water-equivalent material except for the objects shown in Table S1.

TABLE S1
OBJECT GEOMETRY AND MATERIALS OF THE PHANTOM USED IN [1]

Titanium pipe outer radius: 4.445 cm (1.75 inch)			
Titanium pipe inner radius: 4.140 cm (1.63 inch)			
Center x(cm)	Center y(cm)	Radius(cm)	Material
0.3750	0.3750	1.1250	air
-2.2000	-0.5000	0.7500	titanium
1.9000	-0.9000	0.3750	titanium
3.0000	0.0000	0.3000	titanium
-2.2500	1.5000	0.2250	air
0.0000	2.7750	0.0750	air
0.0000	3.0000	0.0750	air
0.2250	3.0000	0.0750	air
-0.2250	3.0000	0.0750	air
0.0000	3.2250	0.0750	air
0.2250	2.7750	0.0750	air
0.4500	2.3250	0.0750	air
0.4500	2.5500	0.0750	air
0.6750	2.5500	0.0750	air
0.2250	2.5500	0.0750	air
0.4500	2.7750	0.0750	air
-0.2250	2.7750	0.0750	air

Continued on next page

TABLE S1 – *Continued from previous page*

Center x(cm)	Center y(cm)	Radius(cm)	Material
-0.4500	2.3250	0.0750	air
-0.4500	2.5500	0.0750	air
-0.6750	2.5500	0.0750	air
-0.2250	2.5500	0.0750	air
-0.4500	2.7750	0.0750	air
2.0250	2.1000	0.0750	air
2.0250	2.3250	0.0750	air
2.2500	2.3250	0.0750	air
1.8000	2.3250	0.0750	air
2.0250	2.5500	0.0750	air
2.2500	2.1000	0.0750	air
2.4750	1.6500	0.0750	air
2.4750	1.8750	0.0750	air
2.7000	1.8750	0.0750	air
2.2500	1.8750	0.0750	air
2.4750	2.1000	0.0750	air
1.8000	2.1000	0.0750	air
1.5750	1.6500	0.0750	air
1.5750	1.8750	0.0750	air
1.3500	1.8750	0.0750	air
1.8000	1.8750	0.0750	air
1.5750	2.1000	0.0750	air
-1.6750	-2.8750	0.0500	air
-1.4250	-2.8750	0.0500	air
-1.1750	-2.8750	0.0500	air
-0.9250	-2.8750	0.0500	air
-1.6750	-2.6250	0.0500	air
-1.4250	-2.6250	0.0500	air
-1.1750	-2.6250	0.0500	air
-0.9250	-2.6250	0.0500	air
-1.6750	-2.3750	0.0500	air
-1.4250	-2.3750	0.0500	air
-1.1750	-2.3750	0.0500	air
-0.9250	-2.3750	0.0500	air
-1.6750	-2.1250	0.0500	air
-1.4250	-2.1250	0.0500	air

Continued on next page

TABLE S1 – Continued from previous page

Center x(cm)	Center y(cm)	Radius(cm)	Material
-1.1750	-2.1250	0.0500	air
-0.9250	-2.1250	0.0500	air
-0.5165	-2.9165	0.0500	air
-0.3495	-2.9165	0.0500	air
-0.1825	-2.9165	0.0500	air
-0.0155	-2.9165	0.0500	air
0.1515	-2.9165	0.0500	air
0.3185	-2.9165	0.0500	air
-0.5165	-2.7495	0.0500	air
-0.3495	-2.7495	0.0500	air
-0.1825	-2.7495	0.0500	air
-0.0155	-2.7495	0.0500	air
0.1515	-2.7495	0.0500	air
0.3185	-2.7495	0.0500	air
-0.5165	-2.5825	0.0500	air
-0.3495	-2.5825	0.0500	air
-0.1825	-2.5825	0.0500	air
-0.0155	-2.5825	0.0500	air
0.1515	-2.5825	0.0500	air
0.3185	-2.5825	0.0500	air
-0.5165	-2.4155	0.0500	air
-0.3495	-2.4155	0.0500	air
-0.1825	-2.4155	0.0500	air
-0.0155	-2.4155	0.0500	air
0.1515	-2.4155	0.0500	air
0.3185	-2.4155	0.0500	air
-0.5165	-2.2485	0.0500	air
-0.3495	-2.2485	0.0500	air
-0.1825	-2.2485	0.0500	air
-0.0155	-2.2485	0.0500	air
0.1515	-2.2485	0.0500	air
0.3185	-2.2485	0.0500	air
-0.5165	-2.0815	0.0500	air
-0.3495	-2.0815	0.0500	air
-0.1825	-2.0815	0.0500	air
-0.0155	-2.0815	0.0500	air
0.1515	-2.0815	0.0500	air
0.3185	-2.0815	0.0500	air
0.6625	-2.9375	0.0500	air
0.7875	-2.9375	0.0500	air
0.9125	-2.9375	0.0500	air
1.0375	-2.9375	0.0500	air
1.1625	-2.9375	0.0500	air
1.2875	-2.9375	0.0500	air
1.4125	-2.9375	0.0500	air
1.5375	-2.9375	0.0500	air
0.6625	-2.8125	0.0500	air
0.7875	-2.8125	0.0500	air
0.9125	-2.8125	0.0500	air
1.0375	-2.8125	0.0500	air

Continued on next page

TABLE S1 – Continued from previous page

Center x(cm)	Center y(cm)	Radius(cm)	Material
1.1625	-2.8125	0.0500	air
1.2875	-2.8125	0.0500	air
1.4125	-2.8125	0.0500	air
1.5375	-2.8125	0.0500	air
0.6625	-2.6875	0.0500	air
0.7875	-2.6875	0.0500	air
0.9125	-2.6875	0.0500	air
1.0375	-2.6875	0.0500	air
1.1625	-2.6875	0.0500	air
1.2875	-2.6875	0.0500	air
1.4125	-2.6875	0.0500	air
1.5375	-2.6875	0.0500	air
0.6625	-2.5625	0.0500	air
0.7875	-2.5625	0.0500	air
0.9125	-2.5625	0.0500	air
1.0375	-2.5625	0.0500	air
1.1625	-2.5625	0.0500	air
1.2875	-2.5625	0.0500	air
1.4125	-2.5625	0.0500	air
1.5375	-2.5625	0.0500	air
0.6625	-2.4375	0.0500	air
0.7875	-2.4375	0.0500	air
0.9125	-2.4375	0.0500	air
1.0375	-2.4375	0.0500	air
1.1625	-2.4375	0.0500	air
1.2875	-2.4375	0.0500	air
1.4125	-2.4375	0.0500	air
1.5375	-2.4375	0.0500	air
0.6625	-2.3125	0.0500	air
0.7875	-2.3125	0.0500	air
0.9125	-2.3125	0.0500	air
1.0375	-2.3125	0.0500	air
1.1625	-2.3125	0.0500	air
1.2875	-2.3125	0.0500	air
1.4125	-2.3125	0.0500	air
1.5375	-2.3125	0.0500	air
0.6625	-2.1875	0.0500	air
0.7875	-2.1875	0.0500	air
0.9125	-2.1875	0.0500	air
1.0375	-2.1875	0.0500	air
1.1625	-2.1875	0.0500	air
1.2875	-2.1875	0.0500	air
1.4125	-2.1875	0.0500	air
1.5375	-2.1875	0.0500	air
0.6625	-2.0625	0.0500	air
0.7875	-2.0625	0.0500	air
0.9125	-2.0625	0.0500	air
1.0375	-2.0625	0.0500	air
1.1625	-2.0625	0.0500	air
1.2875	-2.0625	0.0500	air

Continued on next page

TABLE S1 – Continued from previous page

Center x(cm)	Center y(cm)	Radius(cm)	Material
1.4125	-2.0625	0.0500	air
1.5375	-2.0625	0.0500	air
0.0000	3.7500	0.2032	air
3.2476	-1.8750	0.2032	air
-3.2476	-1.8750	0.2032	air

S2. DERIVATION OF THE DIAGONAL MAJORIZER FOR THE DATA-FITTING OBJECTIVE FUNCTION

For dual material decomposition, one can rewrite the approximate Hessian in (60) in [1] with matrices as follows:

$$\begin{aligned} \tilde{\mathcal{H}}\{\Psi_L^{(q)}\} &= \begin{bmatrix} \mathbf{A}' & 0 \\ 0 & \mathbf{A}' \end{bmatrix} \mathbf{W}^{(q)} \begin{bmatrix} \mathbf{A} & 0 \\ 0 & \mathbf{A} \end{bmatrix} \\ &= \begin{bmatrix} \mathbf{A}' & 0 \\ 0 & \mathbf{A}' \end{bmatrix} \begin{bmatrix} \mathbf{W}_{(1,1)}^{(q)} & \mathbf{W}_{(1,2)}^{(q)} \\ \mathbf{W}_{(1,2)}^{(q)} & \mathbf{W}_{(2,2)}^{(q)} \end{bmatrix} \begin{bmatrix} \mathbf{A} & 0 \\ 0 & \mathbf{A} \end{bmatrix}. \end{aligned} \quad (\text{S1})$$

where $\mathbf{W}_{(l_1, l_2)}^{(q)} = \text{diag}[w_{(i, l_1, l_2)}^{(q)}]_{i=1}^{N_i}$. Note that $\mathbf{W}^{(q)}$ is a block-diagonal, symmetric matrix. We first find the diagonal majorizer of $\mathbf{W}^{(q)}$ using Corollary S2.1 [2] as:

$$\begin{bmatrix} \mathbf{W}_{(1,1)}^{(q)} & \mathbf{W}_{(1,2)}^{(q)} \\ \mathbf{W}_{(1,2)}^{(q)} & \mathbf{W}_{(2,2)}^{(q)} \end{bmatrix} \preceq \begin{bmatrix} \mathbf{W}_{(1)}^{(q)} & 0 \\ 0 & \mathbf{W}_{(2)}^{(q)} \end{bmatrix}, \quad (\text{S2})$$

where $\mathbf{W}_{(l)}^{(q)} = \text{diag}[\sum_{l_2=1}^2 |w_{(i, l_1, l_2)}^{(q)}|]_{i=1}^{N_i}$. By the property of positive semidefinite matrices,

$$\begin{aligned} \begin{bmatrix} \mathbf{A}' & 0 \\ 0 & \mathbf{A}' \end{bmatrix} \begin{bmatrix} \mathbf{W}_{(1,1)}^{(q)} & \mathbf{W}_{(1,2)}^{(q)} \\ \mathbf{W}_{(1,2)}^{(q)} & \mathbf{W}_{(2,2)}^{(q)} \end{bmatrix} \begin{bmatrix} \mathbf{A} & 0 \\ 0 & \mathbf{A} \end{bmatrix} \\ \preceq \begin{bmatrix} \mathbf{A}' & 0 \\ 0 & \mathbf{A}' \end{bmatrix} \begin{bmatrix} \mathbf{W}_{(1)}^{(q)} & 0 \\ 0 & \mathbf{W}_{(2)}^{(q)} \end{bmatrix} \begin{bmatrix} \mathbf{A} & 0 \\ 0 & \mathbf{A} \end{bmatrix} \\ = \begin{bmatrix} \mathbf{A}' \mathbf{W}_{(1)}^{(q)} \mathbf{A} & 0 \\ 0 & \mathbf{A}' \mathbf{W}_{(2)}^{(q)} \mathbf{A} \end{bmatrix}. \end{aligned} \quad (\text{S3})$$

Since (S3) does not have coupled terms between the first and second material fraction images, we can apply the diagonal majorizer [2], [3], [4] to each decoupled matrix.

$$\mathbf{A}' \mathbf{W}_{(l)}^{(q)} \mathbf{A} \preceq \text{diag}[\mathbf{A}' \mathbf{W}_{(l)}^{(q)} \mathbf{A} \mathbf{1}]. \quad (\text{S4})$$

Corollary S2.1. *If \mathbf{B} is a Hermitian matrix, then*

$$\mathbf{B} \preceq \mathbf{D} \equiv \text{diag}[|\mathbf{B}| \mathbf{1}], \quad (\text{S5})$$

where $|\mathbf{B}|$ denotes the matrix consisting of the absolute values of the elements of \mathbf{B} .

Proof. Let $\mathbf{H} \equiv \mathbf{D} - \mathbf{B} = \text{diag}[|\mathbf{B}| \mathbf{1}] - \mathbf{B}$, then

$$\begin{aligned} h_{ii} &= \sum_j |b_{ij}| - b_{ii} \\ &= \left(\sum_{j \neq i} |b_{ij}| \right) + (|b_{ii}| - b_{ii}) \geq \left(\sum_{j \neq i} |b_{ij}| \right), \end{aligned} \quad (\text{S6})$$

because $|b| - b \geq 0$. Also for $j \neq i$: $h_{ij} = -b_{ij}$ so $\sum_{j \neq i} |h_{ij}| = \sum_{j \neq i} |b_{ij}| = h_{ii}$. Thus \mathbf{H} is diagonally dominant so $\mathbf{D} - \mathbf{B} \preceq \mathbf{0}$. \square

S3. COMPARISON OF TWO SIMPLEX PROJECTION SCHEMES IN ONE-DIMENSIONAL PROBLEM

This section provides an example to show how the two projection schemes shown in Fig. 7 in [1] affect the iterative solutions. To simplify, we consider a one-dimensional problem where there is only a single projection data, and a single pixel image. Because of the dual material decomposition, total number of unknown parameters are two; the volume fraction of titanium $f_{(1)}$ and water $f_{(2)}$. We assume noiseless data, so that the iterative solution converges to the true solution in the ideal case.

As a result, the iterative solution with the two-direction projection shown in Fig. S1(d) converges to the true value, but the to-the-closest-point projection shown in Fig. S1(c) keeps rejecting the updates, and the sequence does not converge to the true value.

Note that even with the two-direction projection, there are many cases where the iterative solution does not converge to the true value as the problem is underdefined. However, the volume-fraction-sum constraint still moves the iterative solution closer to the true value, compared to the single material assumption as it finds solution along $f_{(1)} = 0$ only.

S4. LOCAL IMPULSE RESPONSE

This section demonstrates local impulse responses of regularized simple Poisson (SP) and nonlinear Gaussian approximation (NGA) to find regularization parameters that match the resolutions of the reconstructed images. We evaluated local impulse responses with 150 kV, 2 kW source, which has similar photon flux as 20 kW source attenuated by a titanium pipe. Fig. S2 shows the initial impulse shape, and the spatial and frequency responses of the local impulse for regularized SP and NGA. The result shows that the resolutions of regularized SP and NGA are well matched when $\kappa_{(2)} = 3200$ for regularized SP, and $\kappa_{(2)} = 3000$ for regularized NGA.

REFERENCES

- [1] S. Yoon, S. A. Mäkiharju, J. A. Fessler, and S. L. Ceccio, "Image reconstruction for limited angle electron beam x-ray computed tomography with energy-integrating detectors for multiphase flows."
- [2] J. A. Fessler, *Image Reconstruction: Algorithms and Analysis*, ch. Matrices and linear algebra, unpublished manuscript.
- [3] J. Fessler, E. P. Ficaro, N. H. Clinthorne, and K. Lange, "Grouped-coordinate ascent algorithms for penalized-likelihood transmission image reconstruction." *IEEE Trans. Med. Imaging*, vol. 16, no. 2, pp. 166–175, 1997.
- [4] H. Erdogan and J. A. Fessler, "Ordered subsets algorithms for transmission tomography," *Phys. Med. Biol.*, vol. 44, no. 11, p. 2835, 1999.

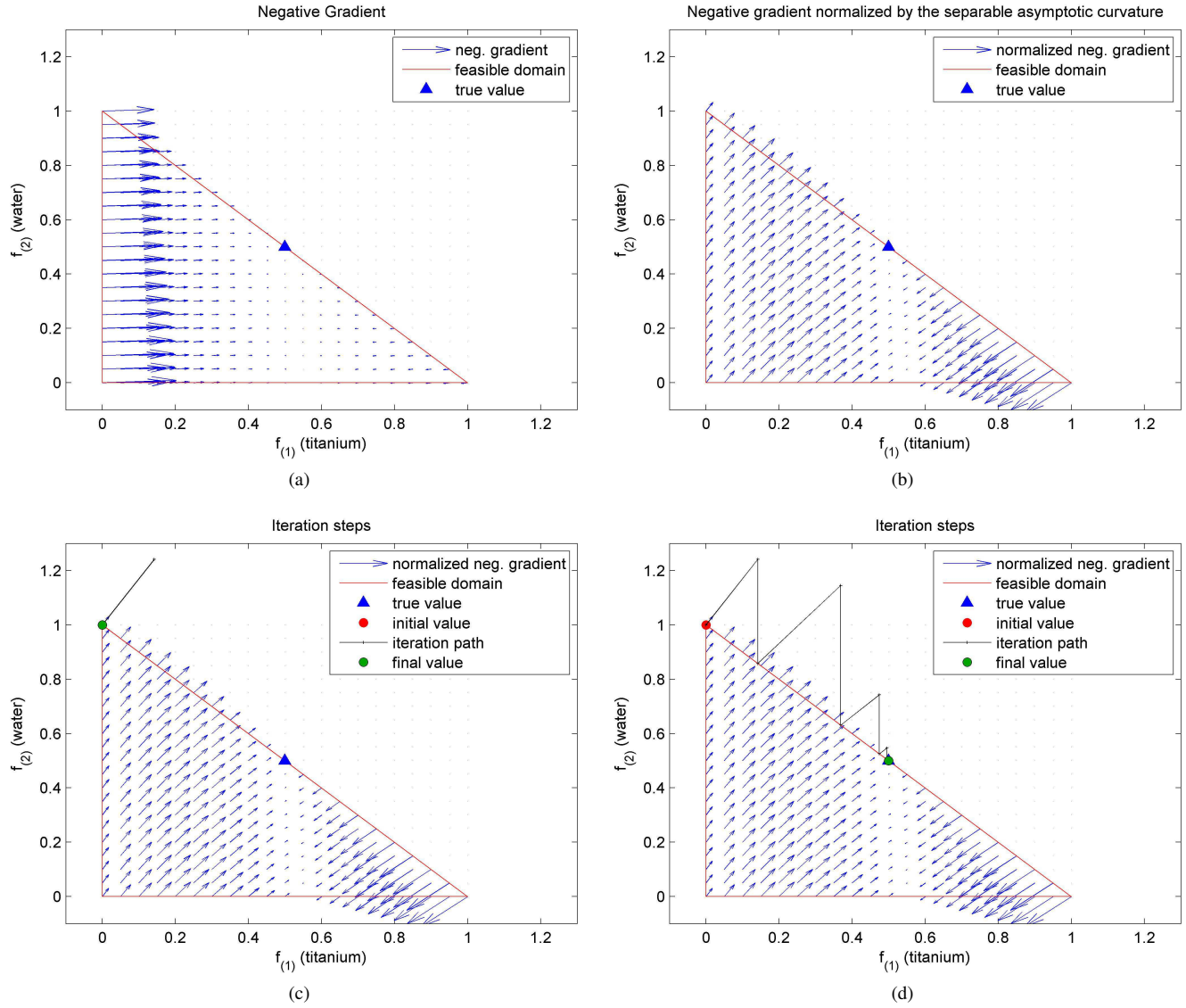


Fig. S1. Iteration sequences for one-dimensional (single ray data - single pixel image) problem with two different projection schemes. (a) negative gradient vector, (b) negative gradient vector normalized by the approximate Hessian, (c) iteration with to-the-closest-point projection, (d) iteration with two-direction projection. True value is $(f_1, f_2) = (0.5, 0.5)$. Data is noiseless.

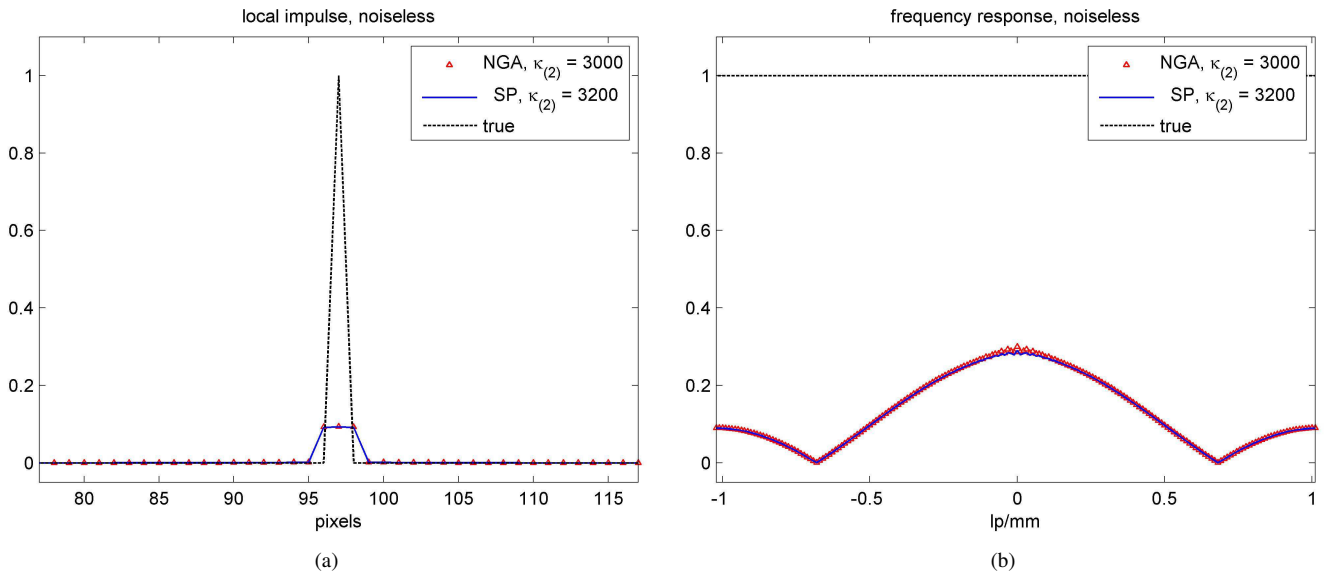


Fig. S2. Local impulse responses of the regularized SP and NGA with 2 kW source; (a) local impulse response in spatial domain, (b) frequency response (absolute).